Parton theory of angle-resolved photoemission spectroscopy spectra in antiferromagnetic Mott insulators

Annabelle Bohrdt,[1,2,*] Eugene Demler,[3] Frank Pollmann,[1,2] Michael Knap,[1,2] and Fabian Grusdt[4,1,2]

[1]*Department of Physics and Institute for Advanced Study, Technical University of Munich, 85748 Garching, Germany*

[2]*Munich Center for Quantum Science and Technology (MCQST), Schellingstr. 4, D-80799 München, Germany*

[3]*Department of Physics, Harvard University, Cambridge, Massachusetts 02138, USA*

[4]*Department of Physics and Arnold Sommerfeld Center for Theoretical Physics (ASC), Ludwig-Maximilians-Universität München, Theresienstr. 37, München D-80333, Germany*

(Received 7 February 2020; revised 7 July 2020; accepted 7 July 2020; published 21 July 2020)

Angle-resolved photoemission spectroscopy (ARPES) has revealed peculiar properties of mobile dopants in correlated antiferromagnets (AFMs). But, describing them theoretically, even in simplified toy models, remains a challenge. Here, we study ARPES spectra of a single mobile hole in the t-J model. Recent progress in the microscopic description of mobile dopants allows us to use a geometric decoupling of spin and charge fluctuations at strong couplings, from which we conjecture a one-to-one relation of the one-dopant spectral function and the spectrum of a constituting spinon in the *undoped* parent AFM. We thoroughly test this hypothesis for a single hole doped into a two-dimensional Heisenberg AFM by comparing our semianalytical predictions to previous quantum Monte Carlo results and our large-scale time-dependent matrix product state calculations of the spectral function. Our conclusion is supported by a microscopic trial wave function describing spinon-chargon bound states, which captures the momentum and t/J dependence of the quasiparticle residue. From our conjecture we speculate that ARPES measurements in the pseudogap phase of cuprates may directly reveal the Dirac-fermion nature of the constituting spinons. Specifically, we demonstrate that our trial wave function provides a microscopic explanation for the sudden drop of spectral weight around the nodal point associated with the formation of Fermi arcs, assuming that additional frustration suppresses long-range AFM ordering. We benchmark our results by studying the crossover from two to one dimension, where spinons and chargons are confined and deconfined, respectively.

DOI: 10.1103/PhysRevB.102.035139

I. INTRODUCTION

The angle-resolved photoemission spectroscopy (ARPES) [1] spectra of doped antiferromagnets (AFMs) have attracted considerable attention. In quasi-one-dimensional (quasi-1D) settings, they have revealed spin-charge separation: Instead of discrete delta-function peaks, a broad continuum signifies the existence of separate branches of a spinless holon and a charge-neutral spinon [2–11]. The situation is strikingly different in the two-dimensional (2D) Heisenberg AFM, the parent compound of high-T_c cuprate superconductors [12]. There, a discrete quasiparticle peak is found in the one-hole ARPES spectrum [13–15], corresponding to a long-lived magnetic polaron [16–35]. For reconciling the experimental observations with numerical calculations in the clean t-J or Hubbard models, inclusion of electron-phonon interactions has been an important issue [36,37]. At finite doping, but before the system becomes superconducting, a pseudogap is observed [38]. Instead of a closed Fermi surface, as might be expected from a Fermi-liquid state, Fermi arcs have been found at low energies around the nodal points $(\pm\pi/2, \pm\pi/2)$ [39] (we use units where the lattice constant $a = 1$ and $\hbar = 1$). These arcs of high spectral weight appear like a part of a small Fermi surface, but the backside of the putative Fermi surface is invisible. The microscopic origin of Fermi arcs in the pseudogap phase of cuprates is not understood today, but their existence has been argued to imply exotic underlying physics and topological order [40–43].

Theoretically predicting ARPES spectra of real solids is challenging. Microscopic models are hard to solve because they involve nontrivial band structures, and electron-phonon and electron-electron interactions; moreover, model parameters are not exactly known. This has led to a long-standing debate about the explanation of ARPES spectra in the undoped AFM insulator and the origin of Fermi arcs.

Here we focus on ARPES spectra in clean toy models for doped AFMs. Even in such idealized scenarios, the theoretical challenges are significant enough that many open questions remain and a universally accepted understanding is lacking. Our work contributes two significant advances: (i) we improve state-of-the-art numerical simulations of ARPES spectra and (ii) we combine our results with recent insights into the microscopic structure of charge carriers in doped AFMs [46,47] obtained from cold-atom experiments with quantum gas microscopes. As a result, we reach a detailed understanding of one-hole ARPES spectra in the paradigmatic t-J model.

*Corresponding author: annabelle.bohrdt@tum.de

Our findings have important consequences, both theoretically and experimentally. Ultracold-atom experiments enable clean studies of the Fermi-Hubbard model with tunable parameters [34,47–52], in 1D or 2D. One can also study continuous dimensional crossovers which are relevant to solids well [53,54]. ARPES spectra can be accessed in optical lattices [55–60], allowing to experimentally test our theoretical predictions in the near future. On the theoretical side, our work verifies that one-hole ARPES spectra in the AFM can be understood from more fundamental constituents (partons), whose properties we can describe on a quantitative and microscopic level. Moreover, this leads to new insights to the current puzzles of cuprates, in particular the microscopic origin of Fermi arcs.

We perform microscopic numerical calculations and study spectral properties of magnetic polarons in the 2D t-J model. On the one hand, we use unbiased time-dependent matrix product state (td-MPS) simulations [61–63] to calculate the one-hole ARPES spectrum on four-leg cylinders [see Fig. 1(a)]. Our work builds upon recent progress in the calculation of dynamical response functions using td-MPSs [64,65]. On the other hand, we use an analytic trial wave function [35] and show that it provides a complete physical picture of the observed low-energy features in the spectrum [see Figs. 1(b) and 1(c) for a summary].

The main results of our paper are as follows. First, we argue that state-of-the-art numerical calculations of the spectral function conclusively demonstrate that magnetic polarons in the clean t-J model are composed of partons: they form mesonlike bound states of spinons and chargons. Second, and in contrast to general wisdom, the spin-charge correlations present in this model at strong coupling can be efficiently described by a Born-Oppenheimer product wave function, *if* one works in the so-called geometric string basis [35,66]. As an important consequence of this second result, we demonstrate that all characteristic low-energy features in the spectrum at strong coupling can be attributed to either spinon or chargon properties. Third, we have a simple analytic understanding of the microscopic chargon properties. This leads us to the main conjecture of our work, namely, that *a one-to-one relation exists, valid at strong coupling, between the observed one-hole spectral function and the spectrum of a constituting spinon in the undoped parent AFM*. This result has consequences well beyond this work, suggesting ARPES spectroscopy at strong coupling as the most direct tool yet to probe the properties of constituting spinons in quantum AFMs. Possible applications include studies of quantum spin liquids.

Our paper is organized as follows. In the remainder of the Introduction, we provide an overview of the main spectral features considered later. We introduce the model Hamiltonian and explain how our results relate to earlier studies. In the following section, we derive the parton theory of ARPES spectra in the geometric string basis. Then, we present our td-MPS results, which contain evidence for the parton nature of magnetic polarons. After establishing the known chargon features in the spectrum, we discuss the rich momentum dependence of the quasiparticle residue $Z(\boldsymbol{k})$ observed at strong couplings. We explain our observations by relating them to spinon properties, which, in turn, we predict by an analytical trial wave function. We close by discussing how our findings

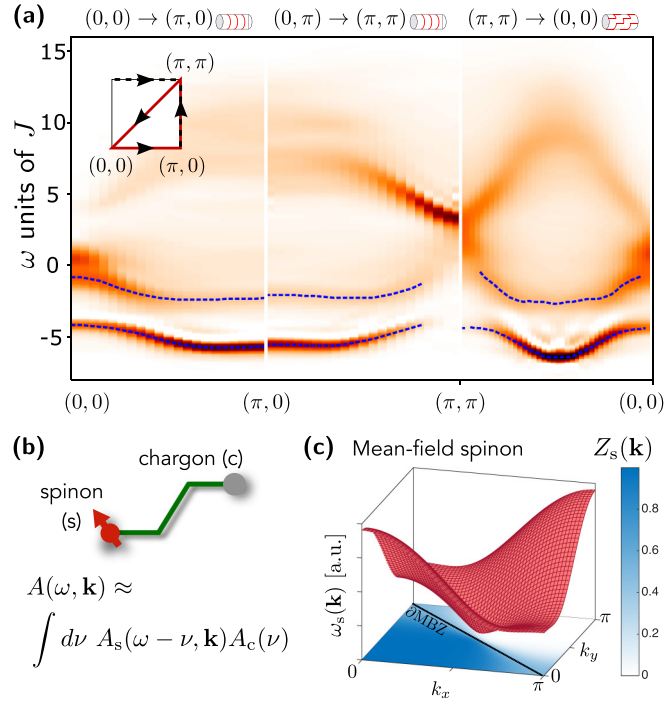

FIG. 1. Magnetic polaron spectra and their unified description. (a) We perform td-MPS simulations of single-hole spectra in the t-J model on 4×40 cylinders of different geometry. At strong couplings $t \gg J$, here $t = 3J$, a strong suppression of spectral weight is observed at (π, π) at low-to-intermediate energies. Details of the td-MPS calculations are provided in Appendix A. The spectrum is obtained along cuts in the Brillouin zone, calculated for different coverings of the cylinder by MPSs (both indicated in the top row). The dashed lines indicate the dispersion relations of the lowest two peaks (determined as local maxima of the spectrum), which we interpret as the ground and first vibrational states of the magnetic polaron. (b) At strong couplings, magnetic polarons can be understood as mesonlike spinon-chargon pairs connected by geometric strings. The spectral function $A(\omega, \boldsymbol{k})$ of a hole can be approximated by a convolution of the spinon and chargon contributions $A_s(\omega, \boldsymbol{k})$ and $A_c(\omega)$, respectively, where the center-of-mass momentum of the meson is carried by the heavy spinon. (c) The optimized slave-particle mean-field theory of fermionic spinons [44,45] yields the correct shape of the magnetic polaron dispersion $\omega_s(\boldsymbol{k})$, with a minimum at the nodal point $(\pi/2, \pi/2)$ and low-energy states along the edge ∂MBZ of the magnetic Brillouin zone. The contribution to the spectral weight $Z_s^{\mathrm{MF}}(\boldsymbol{k})$ predicted by the mean-field spinon ansatz is indicated by the color plot at the bottom. It features a sharp drop at the nodal point $(\pi/2, \pi/2)$, which may be the root of the missing spectral weight on the backside of the Fermi arcs observed in cuprates [39].

may be related to Fermi arcs observed in cuprates, and how related types of experiments on quantum spin liquids can be analyzed in a similar way.

A. Model

In the following we will consider the 2D t-J model, defined by the Hamiltonian $\hat{\mathcal{H}} = \sum_{\mu=x,y} \hat{\mathcal{H}}_t^\mu + \hat{\mathcal{H}}_J^\mu$. It is believed to capture the essential low-energy physics of the anisotropic 2D Fermi-Hubbard model with onsite interaction U and tunnelings t_μ in $\mu = x$ and y directions [67]. The individual terms

are of tunneling type,

$$\hat{\mathcal{H}}_t^{\mu} = -t_{\mu} \sum_j \sum_{\sigma} \hat{\mathcal{P}}_{\mathrm{GW}} \left(\hat{c}^{\dagger}_{j+\boldsymbol{e}_{\mu},\sigma} \hat{c}_{j,\sigma} + \mathrm{H.c.} \right) \hat{\mathcal{P}}_{\mathrm{GW}}, \quad (1)$$

and AFM spin-exchange terms of strength $J_{\mu} = 4t_{\mu}^2/U$,

$$\hat{\mathcal{H}}_J^{\mu} = J_{\mu} \sum_j \left(\hat{\boldsymbol{S}}_{j+\boldsymbol{e}_{\mu}} \cdot \hat{\boldsymbol{S}}_j - \frac{\hat{n}_{j+\boldsymbol{e}_{\mu}} \hat{n}_j}{4} \right). \quad (2)$$

Here, $\hat{c}^{\dagger}_{j,\sigma}$ creates a fermion with spin σ on site $\boldsymbol{j}$, $\boldsymbol{e}_{\mu}$ denotes a unit vector along $\mu = x, y$, and $\hat{\mathcal{P}}_{\mathrm{GW}}$ is the Gutzwiller projector on a subspace with zero or one fermion per lattice site (i.e., the density $\hat{n}_j = \sum_{\sigma} \hat{c}^{\dagger}_{j,\sigma} \hat{c}_{j,\sigma}$ has eigenvalues 0 and 1 only). We mostly focus on the case with exactly one hole, $\sum_j \hat{n}_j = L_x L_y - 1$, with $L_{x,y}$ the linear system size along x and y directions, respectively. If μ is not specified, t and J refer to the isotropic case $t = t_x = t_y$ and $J = J_x = J_y$.

Throughout this paper we work in the strong coupling regime, where $t > J$, but before the Nagaoka polaron regime [68] is reached: $(t/J) < (t/J)_{\mathrm{Nagaoka}}$. Using large-scale density matrix renormalization group (DMRG) [69] simulations, White and Affleck [30] have determined the critical value above which the Nagaoka polaron with a ferromagnetic core is realized, as $(t/J)_{\mathrm{Nagaoka}} = 40 \pm 10$. Note that the motivation for referring to the case $t > J$ as the *strong coupling* regime is the connection of the t-J model, Eqs. (1) and (2), to the Hubbard model with strong onsite interactions U: since the superexchange energy is determined by $J = 4t^2/U$, the Hubbard model's strong coupling regime $U \gg t$ corresponds to $t > J$.

B. Overview and relation to previous works

The magnetic polaron problem of a single hole moving in an AFM background is often considered to be essentially solved. Various semianalytical and numerical techniques have been applied, and many of the key properties of magnetic polarons have been numerically established [16–33]. Nevertheless, there is no agreement on the correct physical interpretation of the obtained results. Partly, this can be attributed to conflicting numerical findings, and disconnected theoretical interpretations of the different features, as we explain next.

In the following, we summarize the main spectral features of a single hole in the 2D t-J model, assuming $t > J$. We focus on low energies, no more than $\approx 2t$ above the one-hole ground state.

(i) At the lowest energies, a dispersive quasiparticle peak, the magnetic polaron, is observed. Its bandwidth is on the order of the superexchange coupling J, rather than hole tunneling t, and the shape of the dispersion relation differs significantly from that of a free hole.

(ii) The quasiparticle residue $Z_{(\pi/2,\pi/2)}$ around the dispersion minimum at the nodal point depends strongly on t/J. All numerical methods have conclusively shown that $Z_{(\pi/2,\pi/2)} > 0$, despite conflicting theoretical proposals [70].

(iii) Above the magnetic polaron ground state, at excitation energies $\Delta E < t$, a second peak has been observed. The most reliable signatures were obtained by Monte Carlo calculations [28,29], while large-scale exact diagonalization studies yielded conflicting results for increasing system sizes [20,26]. Like the ground-state energy E_0 itself, the energy of the first peak E_0 has been shown to be consistent with a scaling of the form $E_n = -2\sqrt{3}t + c_n t^{1/3} J^{2/3}$, asymptotically for $t \gg J$.

(iv) The quasiparticle residue $Z(\boldsymbol{k})$ has strong and nonmonotonic momentum dependence.

Our td-MPS studies confirm (i) and (ii); The resolution afforded by our method allows us to improve the predictions for the position of the first excited peak in (iii) and to study the dependence of $Z(\boldsymbol{k})$ in (iv) for larger values of t/J; moreover, we numerically establish the following additional features see [Fig. 1(a)]:

(v) Around $\boldsymbol{k} = (\pi, \pi)$ the spectral weight is suppressed in a wide window up to energies of order $O(2t)$ above the ground state.

(vi) The first excited peak [see (iii)] can be observed for all momenta, provided the ground-state residue $Z(\boldsymbol{k})$ is nonnegligible. The dispersion relation of the first excited peak is qualitatively identical to the ground state, i.e., the excitation gap $\Delta_{\boldsymbol{k}}$ has only weak $\boldsymbol{k}$ dependence.

Previously, the following theoretical scenarios have been discussed:

(a) *String picture*. Early on, it has been proposed that strings of overturned spins are attached to mobile dopants in a Néel state [32,71–77]. This explains (iii), the scaling of the ground-state energy $E_0 \simeq -2\sqrt{3}t + c_0 t^{1/3} J^{2/3}$ of a single hole at $t \gg J$. The string picture also predicts the existence of vibrationally excited states, whose energies should scale as $E_n = -2\sqrt{3}t + c_n t^{1/3} J^{2/3}$, in accordance with numerical observations [28,29]. Recent ultracold-atom experiments measured spin-spin [46,47] and spin-charge [34] (see also [35]) correlation functions, which also support the string picture. Feature (ii) is also expected from the string picture, owing to the finite length of the strings. Features (i) and (iv)–(vi) require explanations beyond the string picture.

(b) *Parton picture*. Based on phenomenological grounds and numerical evidence, Béran *et al.* [78] proposed the parton picture, in which mobile dopants are described by fractionalized spinons and chargons. In a subsequent work [79], Laughlin drew an analogy with the 1D Fermi-Hubbard model and suggested that the low-energy ARPES spectrum in cuprates can also be interpreted in terms of pointlike spinons and chargons, possibly interacting through a weakly attractive force. The parton picture explains (i): the dispersion relation of the one-hole ground state is determined by the spinon dispersion, which must have a bandwidth $W_{\mathrm{s}} = O(J)$ dominated by spin exchange. The conjectured chargon dispersion, with bandwidth $W_{\mathrm{c}} = O(t)$, is expected to lead to additional features at higher energies in the spectrum. Features (ii) and (iii) are only consistent with the parton picture, if spinons and chargons form a bound state (they could be confined, or form a molecular bound state in a deconfined fractionalized Fermi liquid [80,81]). Scenarios with spin-charge separation as envisioned by Anderson [82], with $Z = 0$ and as found in 1D, can be ruled out numerically [29] at infinitesimal doping. To make quantitative predictions and fully explain features (ii)–(vi), detailed knowledge about the parton dispersions and their microscopic interactions is required; this is typically beyond the scope of phenomenological descriptions. An experimental work [15] has also led to an interpretation of the pronounced

high-energy features in the spectrum as signatures of spinon and chargon branches.

(c) *Polaron picture*. The most widely used microscopic picture so far has been the polaron scenario [16–18,21–25]. As the mobile dopant moves through the AFM, one assumes that it interacts with collective magnon excitations. This picture should not be considered to be separate from (a) and (b): for example, strong interactions with magnons can describe strings of overturned spins attached to the dopant. Spin-wave calculations of the spectral function [21,23] have revealed several vibrational peaks with the expected scaling $\simeq t^{1/3}J^{2/3}$ of their energies [23], thus explaining (iii). The strong renormalization of the bandwidth of the dopant (i), from $O(t)$ to the observed $O(J)$ is also predicted, although without identifying a clear physical mechanism. This is a general disadvantage of the polaron picture: when $t > J$ the system is so strongly coupled that all predictions require advanced numerics or uncontrolled approximations. While the polaron picture per se is certainly correct, it is of little help in the identification of simpler constituents of these polarons.

The goal of this paper is to establish a unifying physical picture, which is able to explain the rich phenomenology (i)–(vi) of the strong coupling ARPES spectrum. We combine the parton and string pictures of magnetic polarons by arguing that the latter are composed of spinons and chargons connected by universal (geometric) strings [see Fig. 1(b)]. Importantly, we provide quantitative descriptions of both ingredients, including a microscopic trial wave function [35,83]. Moreover, we explain why, at strong coupling, any feature of the spectrum is determined by *either* the spinon *or* the chargon/string properties: essentially, a Born-Oppenheimer product ansatz in the geometric string basis [35,66] allows us to factorize spinon and chargon contributions.

As summarized above, the string picture explains features (ii) and (iii). Since we assume that $t \gg J$, we can first neglect the effects of spinon dynamics and describe strings independently. We will demonstrate that the observed strong t/J dependence of the quasiparticle weight (ii) and the excitation energies (iii) can be explained, even quantitatively, by a simple and universal semianalytical calculation. This detailed understanding of the chargon, or equivalently string, properties sets the stage for closer analysis of the spinon properties.

As mentioned above, feature (i) naturally emerges in a parton description of magnetic polarons. Feature (vi) is a direct consequence of the product state nature of the spinon-chargon wave function: the first excited state is a string excitation but shares the same spinon properties as the ground state, including its dispersion relation.

Here, we go beyond earlier phenomenological studies of partons and demonstrate that *quantitative* predictions of the spinon properties are possible. Our starting point is a parton theory of the *undoped* Heisenberg AFM. Specifically, we focus on fermionic U(1) Dirac spinons: These have previously led to accurate variational predictions [44,45] (building upon Anderson's resonating valence bond paradigm [82,84]), and they have recently been proposed to provide a universal description of a larger class of quantum AFMs [85]. For example, the shape of the magnetic polaron dispersion, with its minimum at the nodal point, is inherited from the optimized spinon mean-field state of the Heisenberg AFM [35]. Similar observations were made in Refs. [86,87], but without including geometric strings which are necessary to describe, e.g., features (ii) and (iii).

The mean-field theory we use to describe spinons naturally predicts a strongly momentum-dependent contribution $Z_s(\boldsymbol{k})$ to the quasiparticle weight [see Fig. 1(c)]. Already on the mean-field level, a strong suppression of spectral weight around (π, π) is predicted. Since the low-energy excited states of the magnetic polaron correspond to string excitations, sharing the same spinon contribution $Z_s(\boldsymbol{k})$ to the quasiparticle weight as the ground state, the suppression of spectral weight around (π, π) over a wide energy window is thus explained [feature (v)]. In this work we go beyond the mean-field theory by including a Gutzwiller projection in our trial wave function. As a result, we find nonmonotonic $\boldsymbol{k}$ dependence of $Z(\boldsymbol{k})$ for $t \gtrsim J$, explaining feature (iv), and in excellent agreement with unbiased numerical results.

On the mean-field level, the spinon contribution to the quasiparticle weight $Z_s(\boldsymbol{k})$ exhibits a sudden drop diagonally across the nodal point. This is a direct manifestation of the spinon Dirac cone and reminiscent of the phenomenology of Fermi arcs. In this paper we show that if the system has long-range Néel order and the SU(2) symmetry is spontaneously broken, as in the optimized trial wave function [44,45] we use, the Gutzwiller projection in our magnetic polaron wave function widens the drop of $Z_s(\boldsymbol{k})$ around the nodal point. However, we also show that a sharp drop survives the Gutzwiller projection, if SU(2) invariance is restored in the trial state. This result goes beyond the scope of mean-field parton theories. It may become relevant at finite doping in the t-J model, when frustration restores the SU(2) symmetry. In this regime we thus establish a possible *microscopic* mechanism for the appearance of Fermi arcs, with strongly suppressed spectral weight on the backside of the Fermi pocket. Our microscopic results favor theoretical scenarios in which fermionic spinons and bosonic chargons are the effective constituents of the doped t-J model.

II. RESULTS

A. Parton theory of ARPES spectra

We start by describing the general features of the ARPES spectrum expected from a parton theory of dopants in the 2D t-J model. To simplify the single-occupancy condition built into Eq. (1) we work with the parton, or slave-particle, representation originally introduced in Refs. [88–92]:

$$\hat{c}_{j,\sigma} = \hat{h}_j^\dagger \hat{f}_{j,\sigma}. \tag{3}$$

Here, $\hat{h}_j$ is a chargon operator and $\hat{f}_{j,\sigma}$ denotes a $S = \frac{1}{2}$ spinon operator. The physical Hilbert space is defined by all states satisfying $\sum_\sigma \hat{f}_{j,\sigma}^\dagger \hat{f}_{j,\sigma} + \hat{h}_j^\dagger \hat{h}_j = 1$ for all $\boldsymbol{j}$. Notably, we do not yet have to specify the statistics of $\hat{f}$ and $\hat{h}$, respectively, at this point: both combinations (fermionic spinons and bosonic chargons/bosonic spinons and fermionic chargons) are allowed.

1. Spinon-chargon bound states at strong coupling

We focus on the strong coupling limit $t \gg J$ of the isotropic model, where the fast motion of the hole can

be approximately factorized in the geometric string basis [35,47,66]. We start from the state $|\boldsymbol{j}^{\rm s}\rangle|0\rangle = \sum_\sigma \hat{c}_{\boldsymbol{j}^{\rm s},\sigma}|\Psi_0\rangle$ where a hole is created by removing a fermion on site $\boldsymbol{j}^{\rm s}$ from the ground state $|\Psi_0\rangle$ of the undoped system. This state can be interpreted as a tightly bound state of the spinon and the chargon, both occupying the same site $\boldsymbol{j}^{\rm s}$. Next, we include fast chargon fluctuations. If we properly account for the modified locations of the surrounding spins along the chargon trajectory, the backaction on the spins by the chargon can be neglected if $t \gg J$. This so-called frozen-spin approximation (FSA) [34,47,83] has been shown to be very accurate if the undoped spin system has strong *local* AFM correlations.

Concretely, we introduce an overcomplete set of basis states [35] $|\boldsymbol{j}^{\rm s}\rangle|\Sigma\rangle = \hat{G}_\Sigma(\boldsymbol{j}^{\rm s})|\boldsymbol{j}^{\rm s}\rangle|0\rangle$, where the operator $\hat{G}_\Sigma(\boldsymbol{j}^{\rm s})$ starts at site $\boldsymbol{j}^{\rm s}$ and translates the chargon and spins along the geometric string $\Sigma(\boldsymbol{j}^{\rm s})$:

$$\hat{G}_\Sigma(\boldsymbol{j}^{\rm s}) = \prod_{\langle i,j\rangle\in\Sigma(\boldsymbol{j}^{\rm s})} \left(\hat{h}_i^\dagger \hat{h}_j \sum_{\tau=\uparrow,\downarrow} \hat{f}_{j,\tau}^\dagger \hat{f}_{i,\tau} \right). \tag{4}$$

At strong coupling $t \gg J$, spinon-chargon bound states with center-of-mass momentum $\boldsymbol{k}$ can approximately be described by

$$\left|\Psi_{\rm sc}^{\rm FSA}(\boldsymbol{k})\right\rangle = \frac{1}{L}\sum_{\boldsymbol{j}^{\rm s}} e^{i\boldsymbol{k}\cdot\boldsymbol{j}^{\rm s}} \sum_\Sigma \psi_\Sigma^{\rm FSA} |\boldsymbol{j}^{\rm s}\rangle|\Sigma\rangle. \tag{5}$$

The FSA string wave function $\psi_\Sigma^{\rm FSA}$ ascribes complex amplitudes $\psi_\Sigma^{\rm FSA} \in \mathbb{C}$ to all string configurations Σ. The latter are independent of momentum $\boldsymbol{k}$ and can be calculated from an effective hopping model on the Bethe lattice, with an approximately linear string potential emanating from the spinon position $\boldsymbol{j}^{\rm s}$; see Refs. [35,66] for details. The state in Eq. (5) describes a heavy spinon carrying momentum $\boldsymbol{k}$. The latter binds to itself the light chargon, which is delocalized over a large number of string configurations when $t \gg J$.

Now, we will draw some general conclusions about the ARPES spectrum, assuming that it consists of spinon-chargon eigenstates described by the strong coupling meson wave function in Eq. (5). As a further approximation, valid when the parent state $|\Psi_0\rangle$ has strong local AFM correlations, we assume that the basis states $|\boldsymbol{j}^{\rm s}\rangle|\Sigma\rangle$ are mutually orthonormal: $\langle\boldsymbol{j}^{\rm s\prime}|\boldsymbol{j}^{\rm s}\rangle\langle\Sigma'|\Sigma\rangle \approx \delta_{\boldsymbol{j}^{\rm s\prime},\boldsymbol{j}^{\rm s}}\delta_{\Sigma',\Sigma}$. Otherwise, the following results do not depend on any specific parameters in Eq. (5).

To calculate the spectrum $A(\omega,\boldsymbol{k}) = {\rm Re}\frac{1}{\pi}\int_0^\infty dt\, e^{i\omega t} \times \langle\Psi_0|e^{i\hat{\mathcal{H}}t}(\sum_\sigma \hat{c}_{\boldsymbol{k},\sigma}^\dagger)e^{-i\hat{\mathcal{H}}t}(\sum_\sigma \hat{c}_{\boldsymbol{k},\sigma})|\Psi_0\rangle$, we note that the initial state on the right-hand side is $(\sum_\sigma \hat{c}_{\boldsymbol{k},\sigma})|\Psi_0\rangle = |\boldsymbol{k}^{\rm s}\rangle|\Sigma=0\rangle$, where $|\boldsymbol{k}^{\rm s}\rangle = L^{-1}\sum_{\boldsymbol{j}^{\rm s}} e^{i\boldsymbol{k}^{\rm s}\cdot\boldsymbol{j}^{\rm s}}|\boldsymbol{j}^{\rm s}\rangle$ is a plane-wave spinon state. On the left-hand side, $\langle\Psi_0|e^{i\hat{\mathcal{H}}t} = e^{i\omega_0 t}\langle\Psi_0|$ reduces to a phase factor.

Because of the assumption that spinon-chargon states (5) are eigenstates, we can approximate $e^{-i\hat{\mathcal{H}}t}|\boldsymbol{k}^{\rm s}\rangle|0\rangle \approx e^{-i\hat{\mathcal{H}}_{\rm s}t}|\boldsymbol{k}^{\rm s}\rangle e^{-i\hat{\mathcal{H}}_\Sigma t}|0\rangle$, where $\hat{\mathcal{H}}_{\rm s}$ and $\hat{\mathcal{H}}_\Sigma$ denote effective Hamiltonians of the spinon and string (chargon), respectively. We expect $\hat{\mathcal{H}}_{\rm s} \propto J$ and $\hat{\mathcal{H}}_\Sigma \propto t$ since these terms are dominated by spin-exchange and tunnel couplings, respectively. Explicit forms of $\hat{\mathcal{H}}_{\rm s}$ and $\hat{\mathcal{H}}_\Sigma$ have been derived [34,35,66], and it has been demonstrated that they capture far-from-equilibrium dynamics of a single hole on a remarkable quantitative level [66,93] (see also Ref. [94]).

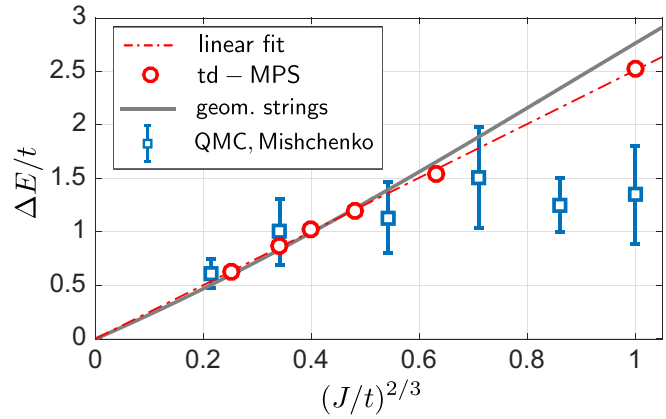

FIG. 2. Scaling of the first vibrational excitation. At strong coupling $t > J$, we analyze the energy ΔE between the lowest two pronounced peaks in the spectrum. Our td-MPS results (red) on $4 \times L_x$ cylinders are compared to quantum Monte Carlo calculations by Mishchenko *et al.* (blue, data extracted from Ref. [29]) and the effective geometric string approach (gray). A fit $\Delta E/t = a(J/t)^{2/3} + b$ to our td-MPS data yields $a = 2.51$ and $b = 2 \times 10^{-3}$. All data are for the ground state at the nodal point $\boldsymbol{k} = (\pi/2, \pi/2)$. See Appendix A for a discussion how the peaks are extracted from our numerically obtained spectra. Finite-size effects in our td-MPS calculations are expected to be weak, but quantitative estimates of their size are difficult.

As a result of the factorization of the eigenstates into spinon-chargon bound states, the spectral function becomes a convolution,

$$A(\omega,\boldsymbol{k})|_{\rm bound} = \int d\nu\, A_{\rm s}(\omega-\nu,\boldsymbol{k})A_{\rm c}(\nu). \tag{6}$$

The spinon contribution $A_{\rm s}(\omega,\boldsymbol{k}^{\rm s}) = {\rm Re}\frac{1}{\pi}\int_0^\infty dt\, e^{i\omega t} \times \langle\boldsymbol{k}^{\rm s}|e^{-i\hat{\mathcal{H}}_{\rm s}t}|\boldsymbol{k}^{\rm s}\rangle$ depends on the momentum $\boldsymbol{k}^{\rm s}$ of the spinon. In contrast, the chargon contribution $A_c(\nu) = {\rm Re}\frac{1}{\pi}\int_0^\infty dt\, e^{i\nu t}\langle\Sigma=0|e^{-i\hat{\mathcal{H}}_\Sigma t}|\Sigma=0\rangle$ is defined in the effective Hilbert space of geometric string states and has no $\boldsymbol{k}$ dependence.

Since $t \gg J$, we can derive the main features of $A_{\rm c}(\nu)$ from a Born-Oppenheimer ansatz where the spinon is assumed to be static. The approximately linear string tension [66] leads to a discrete set of vibrational [71] and rotational [66] states in the spectrum. Because rotational excitations have a node in the center, $|\psi_{\Sigma=0}|^2 = 0$, they do not contribute in the expression for $A_c(\nu)$ and are invisible in ARPES. Indications for the lowest vibrational state have been found in various numerical studies [20,28,29]; we provide further evidence in Figs. 1 and 2. At higher energies, the number of string states per unit of energy grows exponentially. In this regime, self-interactions of the string can lead to hybridization and the formation of a broad continuum, which may explain the absence of higher vibrational peaks in the spectrum.

Because the energy gap to the first vibrational string excitation scales as $\Delta_{\rm c} \simeq t^{1/3}J^{2/3}$ [28,29,71] (see Fig. 2), the low-frequency regime in Eq. (6) is dominated by the spinon

spectrum of width $\simeq J \ll \Delta_c$:

$$A(\omega, \boldsymbol{k}) = A_s(\omega - \nu_c, \boldsymbol{k}) Z_c \quad \text{for } \omega \ll \Delta_c. \tag{7}$$

Here, ν_c is the ground-state energy of the chargon, and Z_c denotes the chargon contribution to the quasiparticle weight. Using the Lehmann representation of $A_c(\nu)$ defined below Eq. (6), we see that Z_c is related to the ground-state string wave function by

$$Z_c = |\psi_{\Sigma=0}|^2. \tag{8}$$

It describes the probability for finding geometric strings of length zero: $\Sigma = 0$. This chargon contribution Z_c depends strongly on the ratio t/J: to see this, we first note that the linear string tension $dE/d\ell \propto J$, proportional to J, causes the binding of the spinon to the chargon. For $dE/d\ell = 0$ the probability for finding strings of length $\ell = 0$ vanishes, $Z_c = 0$; for $dE/d\ell > 0$, this probability increases. Within the FSA and in the considered regime $t \gg J$, the factor Z_c contains the only t dependence of the parton spectrum.

The most important consequence of Eq. (7) is that the entire momentum dependence of the spectrum is captured by the spinon contribution $A_s(\omega, \boldsymbol{k})$ at strong coupling. We expect that the latter exhibits a quasiparticle structure

$$A_s(\omega, \boldsymbol{k}) = Z_s(\boldsymbol{k}) \delta(\omega - \omega_s(\boldsymbol{k})), \tag{9}$$

where $Z_s(\boldsymbol{k})$ denotes the spinon contribution to the quasiparticle residue and $\omega_s(\boldsymbol{k})$ is the spinon dispersion. Combining the last results, we expect the following structure of the ARPES spectrum at low energies:

$$A(\omega, \boldsymbol{k}) = Z_c Z_s(\boldsymbol{k})\, \delta(\omega - \nu_c - \omega_s(\boldsymbol{k})), \quad \omega \ll \Delta_c. \tag{10}$$

In contrast to the chargon properties Z_c and ν_c, which are universally determined by the geometric strings, the spinon properties $Z_s(\boldsymbol{k})$ and $\omega_s(\boldsymbol{k})$ depend on specific properties of the parton model. Hence, one-hole ARPES spectra at strong couplings $t \gg J$ in systems with strong local AFM correlations provide direct information about the properties of constituting spinons in the underlying spin model. Such information is usually extracted from studies of the dynamical spin structure factor [45,65,95], although in that case only pairs of (interacting) spinons can be excited. In the remainder of this paper, we will discuss a microscopic theory constituting spinons in the 2D square-lattice Heisenberg model.

A comment is in order about our notion of *constituting spinons*. If the spin system is in a confining phase, as in the case of the 2D Heisenberg AFM with long-range order, isolated spinon excitations cannot exist: there is no spin-charge fractionalization. The strong coupling parton theory above explicitly assumes, however, that the spinon is bound to the chargon. Such mesonic bound states can exist even in a confining phase. In this case the ARPES spectrum is expected to reveal the properties of the constituting spinon, without the strong renormalization effects present, e.g., in the spin structure factor due to spinon-spinon interactions. In a possible deconfined phase, free-spinon excitations can exist: the constituting spinons are identical to the free spinons in this case. At strong couplings we still expect that spinon-chargon bound states, as described above, will form at low energies. This scenario is realized, e.g., in fractionalized Fermi liquids [80,81], and in this case the ARPES spectrum of the form in Eq. (10) is expected to directly reveal the properties of free spinons.

2. Imperfections

Our parton description of ARPES spectra above was based on the FSA ansatz and assumed strong coupling $t \gg J$. Corrections beyond this idealized scenario are expected: For the 2D t-J_z model it has been shown explicitly that the overcompleteness of the string basis leads to weak renormalization of the spinon properties by the chargon [66] through Trugman loop processes [73]. Similar renormalization is expected to be present in any spin model, but the effect is generically small compared to the string tension [66]. In most models, the latter is of the same order as the spinon bandwidth. We also expect that the dressing of the spinon with the fluctuating geometric string leads to an overall renormalization of the spinon bandwidth $\omega_s(\boldsymbol{k}) \to \omega_s^*(\boldsymbol{k})$. Importantly, at strong couplings such renormalization is independent of the spinon momentum $\omega_s^*(\boldsymbol{k}) = \nu_{FC}\, \omega_s(\boldsymbol{k})$ [35]; ν_{FC} denotes a $\boldsymbol{k}$-independent Franck-Condon factor.

When t and J become comparable, the strong coupling ansatz (5) needs to be modified by including additional correlations. In this case, the center-of-mass momentum $\boldsymbol{k}$ is shared by the partons, and scattering of the chargon on the spinon is expected to renormalize the bound-state dispersion in a $\boldsymbol{k}$-dependent way. Moreover, the overall scale of the dispersion is strongly suppressed compared to the bare dispersion of the constituting spinon, by a Franck-Condon factor $\nu_{FC} \ll 1$ [35].

Finally, magnon corrections are expected to contribute to the ARPES spectrum. While the initial state $(\sum_\sigma \hat{c}_{\boldsymbol{k},\sigma})|\Psi_0\rangle$ is expected to have a large overlap with the one-spinon state considered above, it can also contain spinon-plus-magnon (or three-spinon) contributions. The geometric string introduces couplings of the mesonlike bound state to collective spin-wave, or magnon, excitations in the system. Together these effects lead to polaronic dressing of the spinon-chargon pair, which is expected to reduce the quasiparticle residue $Z_c Z_s(\boldsymbol{k}) \to Z_c Z_s(\boldsymbol{k}) Z_m(\boldsymbol{k})$ and add an incoherent magnon contribution $A_m(\omega, \boldsymbol{k})$ to the idealized spectral function (10). These two effects are related by the sum rule $Z_m(\boldsymbol{k}) + \int d\omega\, A_m(\omega, \boldsymbol{k}) = 1$ for all $\boldsymbol{k}$, which yields an estimate how strongly magnon dressing modifies the parton result.

3. Unbound spinon-chargon pairs

Spin systems in a deconfined phase can also support unbound spinon-chargon pairs. In this case the spectral function also becomes a convolution of a spinon and a chargon (or holon) part. Because the center-of-mass momentum can be distributed arbitrarily between the two partons, the convolution includes both frequency and momentum integrals

$$A(\omega, \boldsymbol{k})|_{\text{unbound}} = \int d\nu\, d\boldsymbol{\kappa}\, A_s(\omega - \nu, \boldsymbol{k} - \boldsymbol{\kappa}) A_c(\nu, \boldsymbol{\kappa}). \tag{11}$$

In the absence of a bound state, the quasiparticle residue $Z = 0$ vanishes, a hallmark of spin-charge separation [96].

The deconfined scenario is realized for example in the 1D t-J model at strong coupling [3,6,9,11]. There, a similar wave function as in Eq. (5) can be used to describe the eigenstates of a single hole [4,97], but the string wave functions

are extended: $\psi_\Sigma^{\rm FSA}(k_c) = e^{-ik_c\Sigma}/\sqrt{L}$ where $\Sigma \in \mathbb{Z}$ denotes linear string configurations of length $\ell_\Sigma = |\Sigma|$ and k_c is the chargon momentum. The spinon wave function in 1D can be accurately modeled by a slave-particle mean-field ansatz for spinons forming a Fermi sea [6,59]. Magnon corrections in 1D have also been calculated and shown to be small [59].

B. Numerical results: td-MPS and DMRG

We use a td-MPS method [61] to calculate the ARPES spectrum in the 2D t-J model on a four-leg cylinder (see Appendix A and Ref. [93] for details). In Fig. 1(a) the spectrum is shown for $t/J = 3$, well within the strong coupling regime but before the Nagaoka effect plays a role [30]. Results for other values of t/J, still in the same regime, are qualitatively similar (see Fig. 9 in Appendix A).

1. Ground state and first vibrational excitation

Consistent with earlier spin-wave [23], exact diagonalization [20,26], truncated basis [32], cluster-perturbation [98], and quantum Monte Carlo calculations [28,29], we find a well-defined quasiparticle peak at low energies. The first vibrational peak above the ground state at the nodal point $(\pi/2, \pi/2)$ is also clearly visible [see Fig. 1(a)]. This peak has been found in earlier quantum Monte Carlo studies, which use analytical continuation to obtain the spectral function [28,29], but the td-MPS method has improved the resolution of the data.

In Fig. 2 we show how the excitation energy ΔE from ground to the first vibrational state depends on the ratio t/J. A linear fit to our MPS data confirms the scaling $\Delta E \propto t^{1/3}J^{2/3}$ at strong coupling with remarkable precision. A parameter-free calculation of the excitation gap using the FSA [35] ansatz (as described Appendix B) is in excellent quantitative agreement with our numerical results.

Owing to the improved resolution of our data, the first vibrational peak is clearly visible in the spectrum for *all* momenta in Fig. 1(a) where the ground-state quasiparticle weight takes appreciable values. Its energy gap $\Delta E(\boldsymbol{k})$ to the ground state is approximately the same for all $\boldsymbol{k}$. The dispersion relation of both peaks follows the expected spinon dispersion [35].

2. Ground-state quasiparticle weight

The residue $Z(\boldsymbol{k})$ of the ground-state quasiparticle peak has a strong momentum dependence, which we attribute to the spinon properties in the parton theory. We find that the spectral weight is strongly suppressed around (π, π), all the way up to large energies $\simeq 2t$ above the ground-state energy. Above this scale, a pronounced dispersive feature is revealed. Outside the magnetic Brillouin zone (MBZ, defined by $|k_x| + |k_y| \leqslant \pi$) we observe a drop of the quasiparticle residue. Later in this paper we will argue that this is a direct signature for fermionic spinon statistics.

Around (0,0) we also find a suppressed quasiparticle weight $Z(0,0) < Z(\pi/2, \pi/2)$, but compared to the situation at (π, π) the effect is less pronounced. More significantly, we find spectral weight in a broad continuum starting slightly above the ground state at (0,0). This should be contrasted with the complete suppression of spectral weight over a wide energy range at (π, π). In addition, the pronounced high-energy feature at (π, π) is completely absent at (0,0). These findings indicate that different mechanisms are responsible for the reduction of spectral weight around (0,0) and (π, π). This finding is further supported by the observation of different t/J dependence at (0,0) and (π, π) (see Fig. 9 in Appendix A).

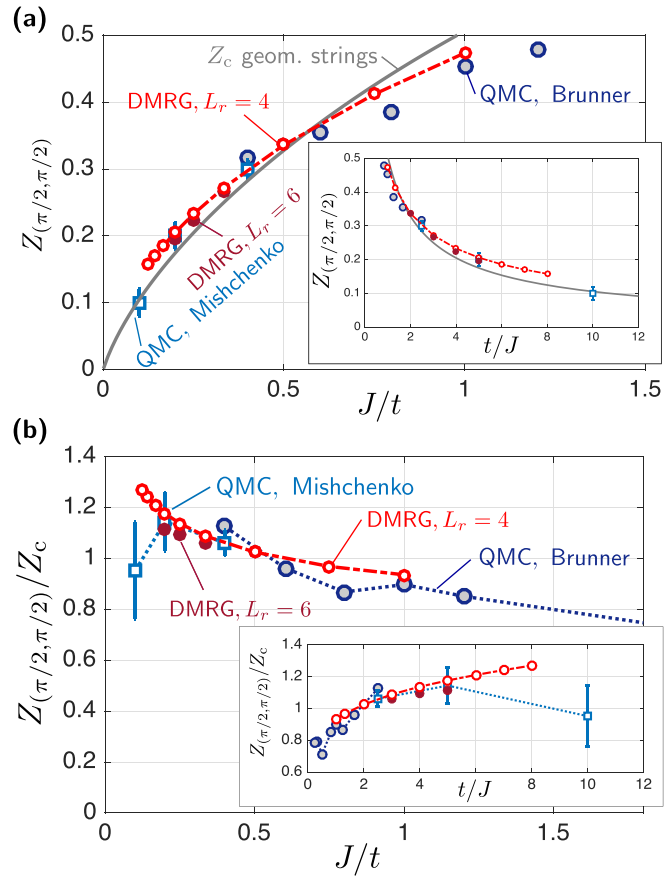

FIG. 3. Ground-state quasiparticle weight and parton contributions. (a) The quasiparticle weight $Z(\pi/2, \pi/2)$ at the nodal point is shown as a function of J/t. We find that earlier numerical Monte Carlo studies by Brunner *et al.* [28] and Mishchenko *et al.* [29] predict values close to the bare chargon, or string, contribution $Z_c = |\psi_{\Sigma=0}^{\rm FSA}|^2$ expected from the geometric string approach (solid gray line). This is confirmed by our DMRG simulations on cylinders with L_r legs: we used bond dimensions $\chi = 500$ ($\chi = 600$) for $L_r = 4$ ($L_r = 6$). (b) We plot $Z_{(\pi/2,\pi/2)}/Z_c$ as a function of J/t. The data show only weak dependence on J/t, indicating that $Z_c(J/t)$ captures the main J/t dependence of the quasiparticle weight; note that for $J/t \lesssim 0.2$ ($t/J \gtrsim 5$) finite-size effects start to become more sizable in the DMRG. The insets show the same data plotted over t/J.

In Fig. 3 we show how the ground-state quasiparticle weight $Z_{(\pi/2,\pi/2)}(J/t)$ at the nodal point depends on the ratio J/t. We compare our DMRG results to earlier quantum Monte Carlo calculations [28,29]. Using DMRG [69] we calculate this quantity from the ground-state wavefunction (see Appendix A). From the parton theory, we expect that $Z \approx Z_c Z_s$ factorizes into chargon, or string, and spinon contributions, Z_c and Z_s respectively [see Eq. (10)]. We also argued that, at strong couplings $t \gg J$, only Z_c depends on the ratio

J/t while $Z_s(\boldsymbol{k})$ only depends on momentum. Now we check this prediction of the parton theory.

In Fig. 3(a) we compare the numerical results directly to $Z_c(J/t) = |\psi^{\mathrm{FSA}}_{\Sigma=0}(J/t)|^2$ which we calculate from the FSA [see Eq. (8)]. Without any free fit parameters, we find that the FSA approach captures correctly the observed J/t dependence, even on a quantitative level (within the observed variations between different theoretical results). This indicates $Z_s(\pi/2, \pi/2) \approx 1$ and additional magnon corrections can be ignored at the nodal point. In Fig. 3(b) this observation is confirmed by plotting $Z_{(\pi/2,\pi/2)}/Z_c$ as a function of J/t, noting that finite-size effects play an increasing role at smaller values of J/t for the DMRG. We find that the behavior of $Z_{(\pi/2,\pi/2)}/Z_c$ is consistent with approaching 1 when $t \gg J$. The dependence of $Z_c(J/t)$ on J/t is discussed in Appendix B.

Except for the features at very high energy $\simeq 2t$ above the ground state, we conclude that the ARPES spectrum at strong coupling can be understood from the general parton theory. In the following, we will focus on the quasiparticle weight $Z(\boldsymbol{k})$ of the magnetic polaron ground state. We will describe a microscopic theory of spinons, chargons, and geometric strings and show that it captures the main features of $Z(\boldsymbol{k})$ observed numerically.

C. Trial wave function

The parton approach can be put on a more solid footing by considering a microscopic trial wave function describing spinon-chargon pairs in the 2D t-J model. We will demonstrate below that its qualitative predictions are in excellent agreement with the numerical results. Some quasiparticle properties predicted by the trial state are rather sensitive to the variational parameters in the wave function, however (see Appendix C), which complicates quantitative predictions for $Z(\boldsymbol{k})$ or the variationally optimal average string length [35].

At quasimomentum $\boldsymbol{k}$, the trial wave function we use describes magnetic polarons with fermionic constituting spinons (slave-boson approach [88–91]) as

$$|\Psi_{\mathrm{sc}}(\boldsymbol{k})\rangle = \sum_{j^s} \frac{\left(u^{(j^s)}_{\boldsymbol{k},\sigma,-}\right)^* e^{i\boldsymbol{k}\cdot j^s}}{L/\sqrt{2}} \times \sum_{\Sigma} \psi_\Sigma \hat{G}_\Sigma \hat{\mathcal{P}}_{\mathrm{GW}} \hat{f}^\dagger_{j^s,\sigma} \left|\Psi^{\mathrm{SF+N}}_{\mathrm{MF}}\right\rangle. \tag{12}$$

We dropped $\hat{h}^\dagger_j$ because the state of the single chargon is fully determined by the Gutzwiller projection; $u^{(j^s)}_{\boldsymbol{k},\sigma,-}$ denotes the cell-periodic part of a Bloch wave function. This ansatz is based on a mean-field model of the Heisenberg AFM with constituting fermionic U(1) Dirac spinons $\hat{f}_{j^s,\sigma}$, which has attracted renewed interest recently [85]. The mean-field state

$$\left|\Psi^{\mathrm{SF+N}}_{\mathrm{MF}}\right\rangle = \prod_{\boldsymbol{k}\in\mathrm{MBZ}} \prod_{\sigma} \hat{f}^\dagger_{\boldsymbol{k},\sigma,-}|0\rangle \tag{13}$$

is a fermionic band insulator [84], where $\hat{f}^\dagger_{\boldsymbol{k},\sigma,\nu}$ creates a spinon with band index $\nu = \pm$. The mean-field spinon dispersion $\omega_s(\boldsymbol{k})$ has been determined variationally [44,45] to be well described by a model with staggered Peierls flux $\pm\Phi$ per plaquette and a staggered Zeeman field $\pm B_{\mathrm{st}}/2$ breaking the SU(2) symmetry [99]

$$\hat{\mathcal{H}}_{f,\mathrm{MF}} = -J_{\mathrm{eff}} \sum_{\langle i,j\rangle,\sigma} \left(e^{i\theta^\Phi_{i,j}} \hat{f}^\dagger_{j,\sigma} \hat{f}_{i,\sigma} + \mathrm{H.c.}\right) + \frac{B_{\mathrm{st}}}{2} \sum_{j,\sigma} (-1)^{j_x+j_y} \hat{f}^\dagger_{j,\sigma} (-1)^\sigma \hat{f}_{j,\sigma}. \tag{14}$$

A trial state related to Eq. (12), but without the geometric strings, has been proposed in Ref. [86].

For the square-lattice Heisenberg AFM with nearest-neighbor (NN) couplings, the optimized variational parameters are $B^{\mathrm{opt}}_{\mathrm{st}}/J_{\mathrm{eff}} = 0.44$ and $\Phi^{\mathrm{opt}} = 0.4\pi$ [45]. In the t-J_z model [100], $B^{\mathrm{opt}}_{\mathrm{st}}/J_{\mathrm{eff}} \to \infty$ and the trial wave function is highly accurate [66]. In the latter case, the Gutzwiller projection becomes obsolete in Eq. (12) because the mean-field state localizes each spin species on a separate sublattice at half-filling.

The $\boldsymbol{k}$-dependent physical properties of the trial wave function can be calculated using variational Monte Carlo sampling [101]. Here, we apply this method to calculate the quasiparticle weight [recall that we dropped $\hat{h}_j$ in Eq. (12) above]

$$Z(\boldsymbol{k}) = \frac{\sum_\sigma \left|\langle \Psi_{\mathrm{sc}}(\boldsymbol{k})|\hat{f}^\dagger_{\boldsymbol{k},\sigma}\hat{\mathcal{P}}_{\mathrm{GW}}\left|\Psi^{\mathrm{SF+N}}_{\mathrm{MF}}\right\rangle\right|^2}{\left|\left\langle\Psi^{\mathrm{SF+N}}_{\mathrm{MF}}\right|\hat{\mathcal{P}}_{\mathrm{GW}}\left|\Psi^{\mathrm{SF+N}}_{\mathrm{MF}}\right\rangle\langle\Psi_{\mathrm{sc}}(\boldsymbol{k})|\Psi_{\mathrm{sc}}(\boldsymbol{k})\rangle\right|}, \tag{15}$$

where the denominator guarantees proper normalization. Our Monte Carlo procedure for sampling (15) is explained in Appendix C.

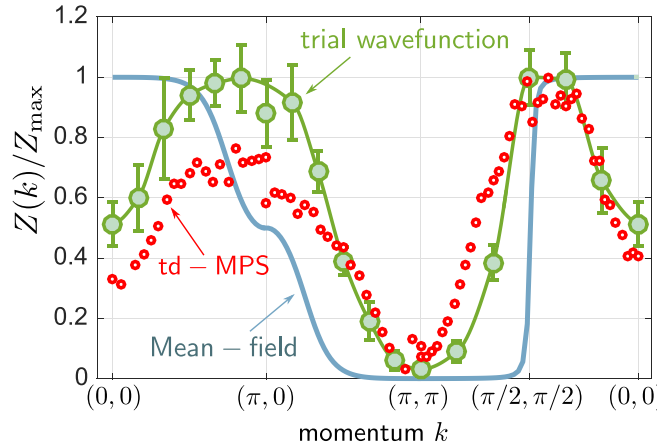

FIG. 4. Momentum dependence of the quasiparticle weight. We calculate the quasiparticle residue $Z(\boldsymbol{k})$, normalized by $Z_{\max} = \max_{\boldsymbol{k}} Z(\boldsymbol{k})$, from the trial wave function (12) along a cut $(0,0) - (\pi,0) - (\pi,\pi) - (0,0)$ in a periodic 12×12 system. Parameters are $t = 3J$ and we used the optimized mean-field parameters $B_{\mathrm{st}}/J_{\mathrm{eff}} = 0.44$ and $\Phi = 0.4\pi$. The solid green line is a guide to the eye. We compare our results to the bare mean-field prediction (solid blue line) and results from our td-MPS calculations (red dots). See Appendix A for how $Z(\boldsymbol{k})$ is numerically extracted from td-MPS.

Results

In Fig. 4 we plot the $\boldsymbol{k}$ dependence of the quasiparticle weight Z of the trial wave function. We set $t = 3J$, in the strong coupling regime, and used the string wave function

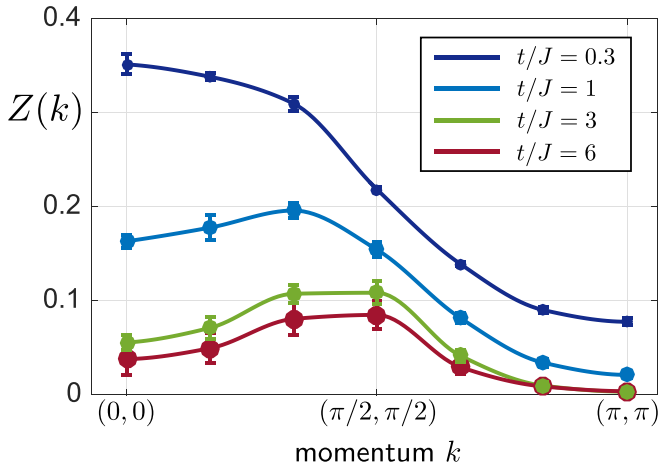

FIG. 5. Dependence on t/J. Using the trial wave function (12) with $\psi_\Sigma = \psi_\Sigma^{\mathrm{FSA}}$ we calculate the quasiparticle weight $Z(\boldsymbol{k})$ along the diagonal cut $(0,0)-(\pi,\pi)$ for different values of t/J. We set $B_{\mathrm{st}}/J_{\mathrm{eff}} = 0.44$ and $\Phi = 0.4\pi$ in a 12×12 system; solid lines are guides to the eye.

$\psi_\Sigma = \psi_\Sigma^{\mathrm{FSA}}$ obtained from the FSA in Eq. (12). We checked that no significant dependence on system size remains (see Appendix C).

The comparison with our numerical td-MPS results shows that the trial wave function correctly predicts the qualitative features: in the center of the MBZ, around (0,0), we observe a dip of the spectral weight. The maximum is found at the edge of the MBZ, including at the high-symmetry points $(\pi,0)$ and $(\pi/2,\pi/2)$. Outside the MBZ, the Z factor is strongly suppressed: at (π,π) we calculate that it drops below 10^{-2}. Overall we observe a strong momentum dependence of the Z factor, which is qualitatively captured by the trial wave function. The latter includes strong $\boldsymbol{k}$ dependence as a consequence of the Fermi statistics that determine the spinon properties in the trial state.

In Fig. 5 we study the dependence of the quasiparticle weight $Z(\boldsymbol{k})$ on t/J, along the diagonal cut $(0,0)-(\pi,\pi)$. Here, t/J controls the length distribution of the geometric strings Σ which we use in the FSA string wave function $\psi_\Sigma = \psi_\Sigma^{\mathrm{FSA}}$ in Eq. (12). Overall, the spectral weight decreases when t/J is increased, as expected from Eqs. (7) and (8) on general grounds. In addition, a nontrivial momentum dependence develops as t/J is increased: for small t/J the spectral weight around (0,0) is enhanced, but it is suppressed for large t/J. The same qualitative behavior is observed in our td-MPS simulations (see Fig. 9 in Appendix A).

The J/t dependence of Z observed in Fig. 5 at the nodal point $(\pi/2,\pi/2)$ is also significant. As expected, we observe a decrease in $Z_{(\pi/2,\pi/2)}$ as t/J increases. In comparison with the data shown in Fig. 3, the overall magnitude of the quasiparticle weight in the trial wave function is too small by a factor of about 2. We note, however, that the quasiparticle residue depends much more sensitively on the parameters in the trial wave function than, for example, the corresponding variational energy [35]. As discussed in more detail in Appendix C, the quasiparticle weight is sensitive to the staggered field $B_{\mathrm{st}}/J_{\mathrm{eff}}$ and the string tension used to calculate ψ_Σ in Eq. (12). We believe this is the main reason for the observed deviations.

D. Mean-field approximation

A mean-field description of the constituting spinons is obtained by dropping the Gutzwiller projection in Eqs. (12) and (15) and working directly with the mean-field Hamiltonian from Eq. (14). In principle, bosonic [92] or fermionic [88–91] spinons can both be considered. However, the bosonic theory would require strong interactions to explain the observed spinon quasiparticle weight $Z_{\mathrm{s}}(\boldsymbol{k}) \approx Z(\boldsymbol{k})/Z_{\mathrm{c}}$. We will argue that noninteracting fermionic spinons readily predict the qualitative features of $Z_{\mathrm{s}}(\boldsymbol{k})$.

1. Fermionic spinons

We calculate $Z^{\mathrm{MF}}(\boldsymbol{k})$ by applying the FSA and mean-field approximations in Eq. (15). First, we note that $\boldsymbol{k}$ is an arbitrary vector from the full Brillouin zone (BZ); spinon operators $\hat{f}_{\boldsymbol{k},\sigma}$ are defined in the BZ, whereas for spinons $\hat{f}_{\boldsymbol{k},\sigma,\nu}$ with band indices ν the cases $\boldsymbol{k}\in$ MBZ and $\boldsymbol{k}\notin$ MBZ have to be distinguished.

In the FSA we assume that only the trivial string state $\Sigma = 0$ contributes since nontrivial string states are approximately orthogonal to the background AFM. Then, dropping the Gutzwiller projections yields

$$Z^{\mathrm{MF}}(\boldsymbol{k}) = Z_{\mathrm{c}} \sum_\sigma \left|\left\langle \Psi_{\mathrm{MF}}^{\mathrm{SF+N}}\right| \hat{f}^\dagger_{\boldsymbol{k},\sigma,-}\hat{f}_{\boldsymbol{k},\sigma}\left|\Psi_{\mathrm{MF}}^{\mathrm{SF+N}}\right\rangle\right|^2. \tag{16}$$

This expression is of the general form expected from the parton theory [see Eq. (10)]. The spinon contribution on the right-hand side of Eq. (16) is related to the mean-field Bloch wave function $u^{(A,B)}_{\boldsymbol{k},\sigma,-}$ for sites $\boldsymbol{j}$ from the A and B sublattice, respectively (see Appendix D):

$$Z_{\mathrm{s}}^{\mathrm{MF}}(\boldsymbol{k}) = \frac{1}{2}\sum_\sigma \begin{cases} \left|u^{(A)}_{\boldsymbol{k},\sigma,-} + u^{(B)}_{\boldsymbol{k},\sigma,-}\right|^2, & \boldsymbol{k}\in \mathrm{MBZ} \\ \left|u^{(A)}_{\boldsymbol{k},\sigma,-} - u^{(B)}_{\boldsymbol{k},\sigma,-}\right|^2, & \text{else.} \end{cases} \tag{17}$$

One important conclusion is that $Z_{\mathrm{s}}^{\mathrm{MF}}(\boldsymbol{k})$ generally reflects the $\boldsymbol{k}$ dependence of the Bloch wave functions, which is determined by the parameters $B_{\mathrm{st}}/J_{\mathrm{eff}}$ and Φ in the mean-field Hamiltonian (14). Moreover, momenta within the MBZ and outside of it are treated separately, causing constructive and destructive interference of the Bloch wave functions respectively.

In the following limiting cases the mean-field spinon contribution $Z_{\mathrm{s}}^{\mathrm{MF}}(\boldsymbol{k})$ shows interesting behavior. In a classical Néel state, when $B_{\mathrm{st}}/J_{\mathrm{eff}}\to\infty$, it holds $(u^{(A)}_{\boldsymbol{k},\sigma,-}, u^{(B)}_{\boldsymbol{k},\sigma,-}) = (1,0)$ or $(0,1)$. This leads to a featureless spinon spectrum $Z_{\mathrm{s}}^{\mathrm{MF}}(\boldsymbol{k}) = 1$ everywhere [see Fig. 6(a)]. For the uniform resonating valence bond state $\Phi = 0$ and $B_{\mathrm{st}} = 0$, it holds $u^{(A)}_{\boldsymbol{k},\sigma,-} = u^{(B)}_{\boldsymbol{k},\sigma,-} = 1/\sqrt{2}$. The constituting spinons form a Fermi sea occupying the MBZ, which is directly reflected by the strongly asymmetric spectral weight: $Z_{\mathrm{s}}^{\mathrm{MF}}(\boldsymbol{k}) = 2$ for $\boldsymbol{k}$ within MBZ, and $Z_{\mathrm{s}}^{\mathrm{MF}} = 0$ otherwise [see Fig. 6(b)]. When $B_{\mathrm{st}} = 0$ but the staggered magnetic flux $\Phi\neq 0$, the mean-field dispersion has a Dirac cone around the nodal point $\boldsymbol{k} = (\pi/2,\pi/2)$. This leads to a shard drop of spectral weight along the diagonal from (0,0) to (π,π) crossing the Dirac point [see Fig. 6(c)].

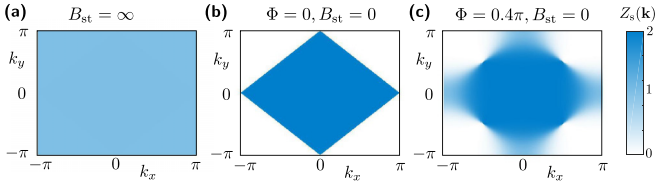

FIG. 6. Mean-field spinon contribution to the quasiparticle residue. $Z_s^{MF}(\boldsymbol{k})$ from Eq. (17) is shown in the following limiting cases: (a) $B_{st}/J_{eff} \to \infty$, (b) $B_{st} = \Phi = 0$, (c) $B_{st} = 0$ and $\Phi = 0.4\pi$. The color bar is indicated on the right.

For the mean-field parameters B_{st}/J_{eff} and Φ optimized for the half-filled Heisenberg AFM [45] the mean-field spinon spectral weight is plotted in Fig. 1(c) (color scale) and in Fig. 4. We observe a sharp drop of $Z_s^{MF}(\boldsymbol{k})$ around the nodal point, although the weak staggered field leads to some broadening. Around $(0, \pi)$ and $(\pi, 0)$, the decrease of the spectral weight is smoother, which we attribute to the larger distance in $\boldsymbol{k}$ space from the Dirac cone found at the nodal point for $B_{st} = 0$.

Overall, the $\boldsymbol{k}$ dependence of the quasiparticle weight from the mean-field parton theory $Z^{MF}(\boldsymbol{k}) = Z_c Z_s^{MF}(\boldsymbol{k})$ captures the numerical observations. In particular, it explains the strong suppression of spectral weight around (π, π), extending up to high energies, as a direct signature of fermionic spinon statistics. Other features observed numerically, such as the more pronounced broadening of spectral weight around the edge of the MBZ and the suppressed quasiparticle residue at (0,0) can be attributed to the Gutzwiller projection and effects beyond FSA. As shown above, these features are correctly predicted by the trial wave function (12).

2. *Bosonic spinons*

So far, we only described the case where the constituting spinons have fermionic statistics. However, using Schwinger bosons, the Heisenberg AFM can also be described by bosonic constituting spinons (see, e.g., Ref. [67]). As described in Appendix D, the trial wave function from Eq. (12) can be adapted to the bosonic case. On the mean-field level one finds that the spinon contribution to the quasiparticle residue contains two delta-function peaks of equal weight around $\boldsymbol{k} = (0, 0)$ and (π, π). This observation is inconsistent with unbiased numerical results, where $Z(\boldsymbol{k})$ is strongly suppressed around $\boldsymbol{k} = (\pi, \pi)$. Thus, our results favor parton theories with fermionic constituting spinons, although it is difficult to rule out scenarios with bosonic spinons and strong interaction effects suppressing $Z_{(\pi,\pi)}$.

E. Dimensional crossover

Now, we subject the parton theory to another test and study ARPES spectra in the dimensional crossover. We tune the ratio

$$\alpha = t_y/t_x \tag{18}$$

of tunneling amplitudes along x and y directions, which leads to spin-exchange couplings $J_y = \alpha^2 J_x$. In ultracold-atom experiments with optical lattices, the value of α can be easily tuned.

Our main motivation for considering the dimensional crossover is that the parton theory with fermionic spinons correctly describes the ARPES spectrum in the 1D t-J model [6,59]. For nonzero $\alpha > 0$ we expect a nonvanishing string tension $\propto \alpha J_x$ which should lead to spinon-chargon binding. At $\alpha = 1$ we have established above that the parton theory can explain the numerically observed spectra.

In the 1D case, spinons and chargons are deconfined and unbound for $t \gg J$. Because the spectrum is a convolution of spinon and chargon contributions both in momentum and frequency domains [see Eq. (11)], a coherent quasiparticle peak is absent. Nevertheless, the integrated spectral weight $Z_\omega(k) = \int_0^{\Delta\omega} d\nu\, A[\nu_0(k) + \nu, k]$ in a low-energy region of width $\Delta\omega = O(J)$ around the ground state at $\nu_0(k)$ reveals the structure of the spinon Fermi sea. Because $t \gg J$, only chargon states from a narrow range of momenta Δk_c around the minimum at $k_c = 0$ of the chargon dispersion $\nu_c(k_c) = -2t\, \cos(k_c)$ contribute to $Z_\omega(k)$ [102]. In one dimension, the mean-field parton theory for the optimized parameter $B_{st} = 0$ in Eq. (14) predicts a step function [see Eq. (17)]

$$Z_s^{MF}(k) = \begin{cases} 2, & |k| \leqslant \pi/2 \\ 0, & \text{else} \end{cases} \tag{19}$$

which directly reflects the Fermi-Dirac distribution of spinons in the ground state [6,59].

In 1D, the above argument predicts a strong suppression of spectral weight up to energies of order $O(2t) \gg J$ around $k = \pi$, which has been observed numerically [5,9,59]. As discussed earlier, we find the same phenomenology around $\boldsymbol{k} = (\pi, \pi)$ in two dimensions, where we also attributed the effect to the underlying fermionic spinon statistics in the mean-field parton theory. To further support our argument that the 1D and 2D cases are due to the same physical principle, now we demonstrate that they continuously evolve into each other in a dimensional crossover.

In Fig. 7(a) we show our numerical td-MPS results for values of $\alpha = \frac{1}{3}$, $\frac{2}{3}$, and 1. We consider three cuts along diagonals $k_y = k_x + k_y^{(0)}$ with $k_y^{(0)} = \pi, \pi/2$ and 0. For $\alpha = \frac{1}{3}$ the spectrum still closely resembles the 1D case, and only a weak dependence on k_y is observed: The minima of the ground-state dispersion in the second cut, corresponding to $k_y^{(0)} = \pi/2$, are slightly displaced to the left of $k_x = \pm\pi/2$, as expected from the mean-field spinon dispersion shown in Fig. 7(b). While some spectral weight appears at $\boldsymbol{k} = (\pi, 0)$ (first cut with $k_y^{(0)} = \pi$), it remains absent over a broad energy range at $\boldsymbol{k} = (\pi, \pi)$ (third cut with $k_y^{(0)} = 0$). In general, the high-energy features can still be understood from a theory of quasifree spinons and chargons as in 1D.

For $\alpha = \frac{2}{3}$ a well-defined quasiparticle peak is visible at low energies. This is expected from the parton theory, which predicts the formation of a spinon-chargon bound state as soon as the string tension $\propto J_y$ becomes sizable. Around $\boldsymbol{k} = (\pi, \pi)$ we still observe a strong suppression of spectral weight over a wide energy range of order $O(2t_x)$. The dispersive features at high energies, reminiscent of a free chargon branch, become increasingly less pronounced as α approaches 1.

In Fig. 7(b) we plot the mean-field spinon dispersion expected for the dimensional crossover. While the overall scale is difficult to predict, the shape of the spinon dispersion

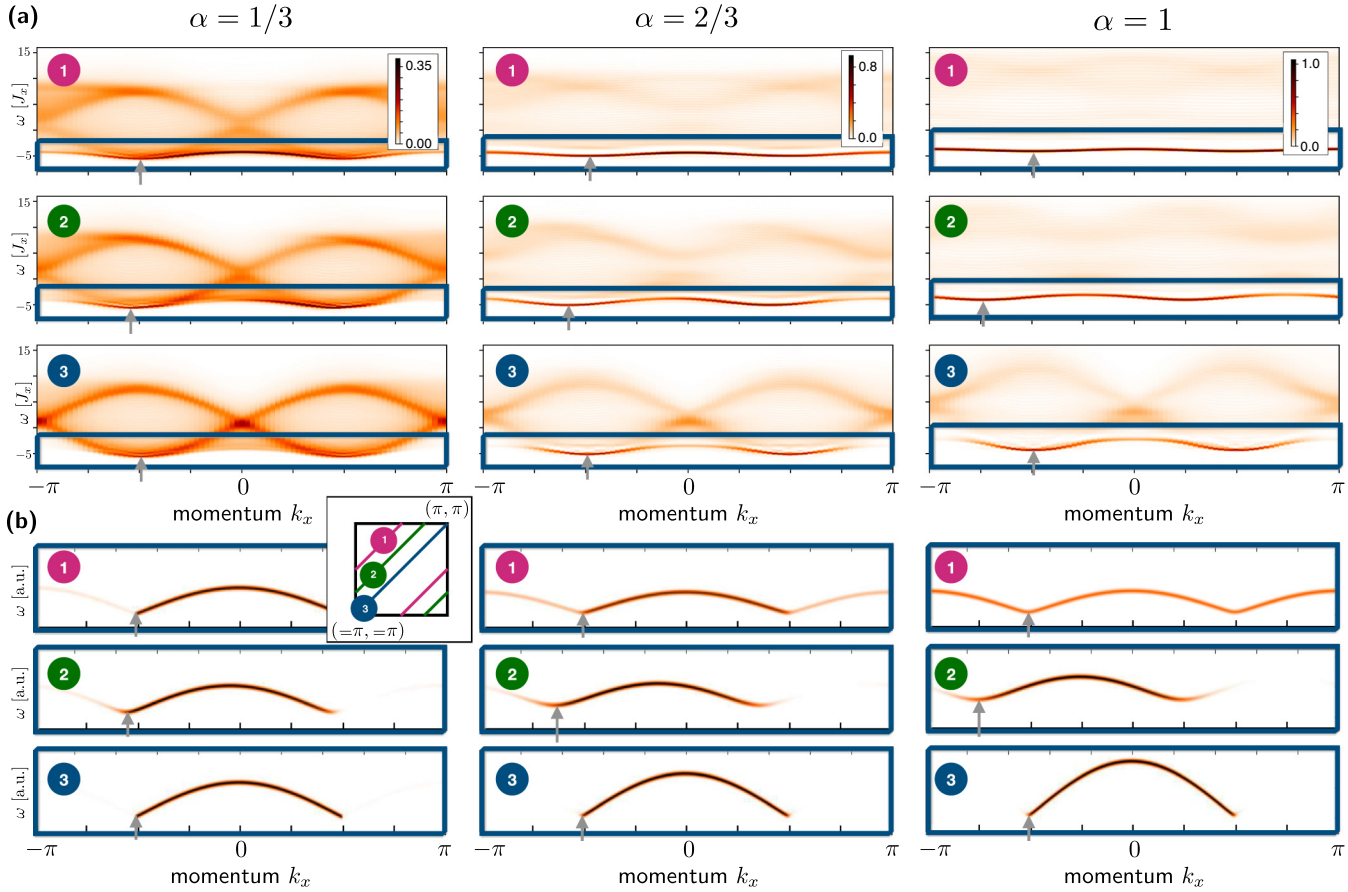

FIG. 7. One-hole spectral function in the dimensional crossover. (a) For varying anisotropy $\alpha = t_y/t_x$ (indicated in top row) of the hopping elements, and $\alpha^2 = J_y/J_x$ of the superexchange couplings, we use td-MPS to calculate the spectral function. We consider cylinders of length $L_x = 40$ along x, with circumference $L_y = 4$ along the periodic y direction; $t_x/J_x = 3$ is fixed. The MPS is wrapped around the cylinder along diagonals, which allows us to calculate diagonal cuts: $k_y = k_x + k_y^{(0)}$ with $k_y^{(0)} = \pi, \pi/2, 0$ (cuts 1,2,3, see inset below left panel). (b) Predictions for the spinon contribution Z_s to the spectral weight (color map) and dispersion from fermionic mean-field theory of spinons, as described in the text. Mean-field parameters are taken from Ref. [83]. The delta-function peaks are represented by broadened lines with integrated weight equal to $Z_s(\boldsymbol{k})$. In (a) and (b) the locations of dispersion minima in the low-energy region (blue boxes) are indicated by gray arrows.

resembles the numerically observed quasiparticle dispersion [the low-energy onset of the spectrum in Fig. 7(a)] for all considered values of α. The variational mean-field parameters $B_{\rm st}(\alpha)$ and $\Phi(\alpha)$ have been taken from Ref. [83]. The color scale in Fig. 7(b) indicates the spinon quasiparticle weight $Z_s^{\rm MF}(\boldsymbol{k})$. Around the nodal point $\boldsymbol{k} = (\pi/2, \pi/2)$ the numerically obtained spectrum, as a function of momentum, evolves significantly more smoothly than expected from the mean-field theory. We attribute this to the effect of the Gutzwiller projection neglected in the mean-field calculation, as discussed earlier for the 2D case. Around $\boldsymbol{k} = (\pi, \pi)$ the mean-field theory correctly predicts the strongly suppressed quasiparticle weight at all values of α. We conclude that the parton theory correctly predicts the observed qualitative features of the ARPES spectrum in the dimensional crossover.

F. Frustrated magnetism: Dirac spin-liquid scenario

The main signature of fermionic spinon statistics we reported so far was indirect and based on the suppression of spectral weight around $\boldsymbol{k} = (\pi, \pi)$. Now, we use our trial wave function and discuss a case where direct signatures for the formation of fermionic Dirac spinons can be observed. These considerations are relevant to doped quantum magnets with additional frustration. Which spin liquid is relevant depends on the type of frustration, and in many cases this is subject of debate. Here, we restrict ourselves to the Dirac spin-liquid case captured by our trial wave function, while different signatures can be expected for other quantum spin liquids [103–105].

On the level of the mean-field theory in Eq. (14), the spin liquid without Néel order is realized when $B_{\rm st} = 0$ and a nonvanishing staggered flux $\Phi \neq 0$ is considered. This leads to the formation of Dirac cones at the nodal point $\boldsymbol{k} = (\pi/2, \pi/2)$, across which the mean-field approach predicts a sudden drop of the spinon quasiparticle weight [see Fig. 6(c)]. Now, we will go beyond the mean-field approximation and demonstrate that the trial wave function (12), including the Gutzwiller projection, exhibits the same features.

So far, we studied spinon-chargon pairs in a background with long-range Néel order, characterized by $B_{\rm st} \neq 0$ in the trial wave function. Even in the strong coupling regime, where $t \gg J$, we found that the spectral weight $Z(\boldsymbol{k})$ decays smoothly along the diagonal from $\boldsymbol{k} = (\pi/2, \pi/2)$ to (π, π)

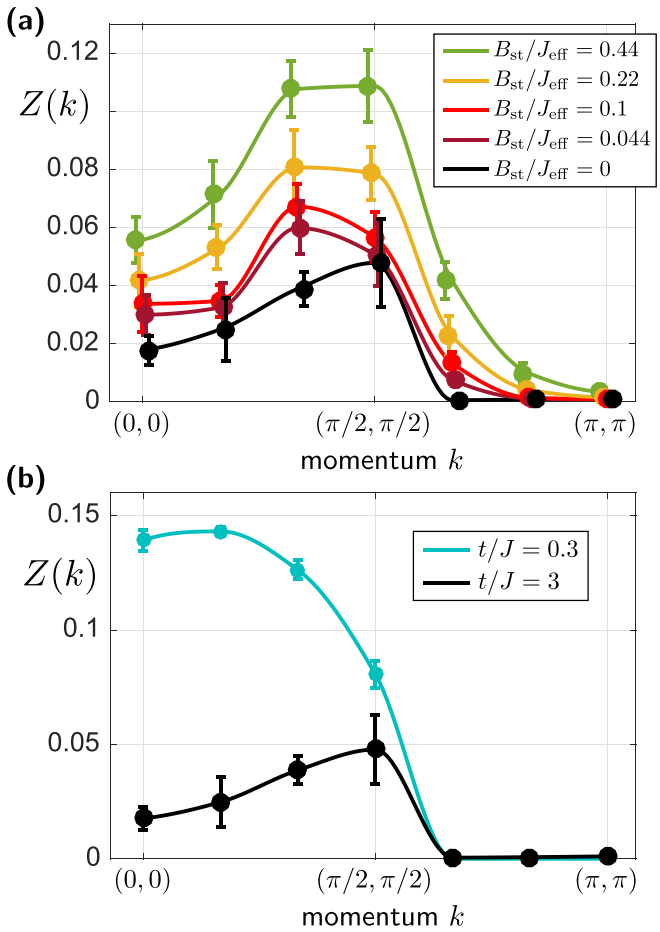

FIG. 8. Quasiparticle weight $Z(k)$ for a Dirac quantum spin-liquid scenario, along the diagonal cut from (0,0) to (π,π). (a) When the long-range AFM order in the trial wave function, controlled by B_{st}/J_{eff}, is reduced, a sudden drop develops around the edge of the MBZ at $(\pi/2,\pi/2)$. Such behavior can be expected if a Dirac quantum spin liquid emerges upon frustrating spin-exchange interactions in the t-J model. This scenario can be described qualitatively by the mean-field theory of fermionic spinons. We used $t/J = 3$ and $\Phi = 0.4\pi$ in our trial wave function; at each momentum data points are slightly offset horizontally for better visibility. (b) For $B_{st} = 0$ and a large range of t/J we observe a sharp drop of spectral weight around the nodal point. In (a) and (b) the solid lines are guides to the eye only.

in 2D (see, e.g., Figs. 4 and 5). While a small amount of broadening is expected even on the mean-field level when $B_{st} \neq 0$, most of the effect is due to the Gutzwiller projection in the trial state.

In Fig. 8(a) we show how the quasiparticle weight $Z(\boldsymbol{k})$ of the trial wave function depends on the staggered field B_{st}. In addition to an overall decrease in magnitude, the formation of a sharp feature at the edge of the MBZ is observed when B_{st} is decreased. For a hole moving in the SU(2)-invariant U(1) Dirac spin liquid with $B_{st} = 0$ and $\Phi = 0.4\pi$, we find that $Z(\boldsymbol{k}) = 0$ vanishes within error bars for momenta along the diagonal beyond the nodal point, with $|\boldsymbol{k}| > \pi/\sqrt{2}$. This behavior can be understood from the mean-field theory as a direct signature for (i) the formation of a Dirac cone at the nodal point and (ii) fermionic spinon statistics. Importantly, the behavior persists even though spinons and chargons in the trial wave function remain bound.

The sudden drop of the quasiparticle weight around the nodal point is reminiscent of the missing spectral weight on the backside of the Fermi arcs observed in the pseudogap phase of cuprates [39]. A similar effect has been observed in a doped spin liquid on the kagome lattice, believed to exhibit spin-charge separation [106]. Within our microscopic approach, the strong suppression of the quasiparticle residue in the vicinity of the nodal point, but outside the MBZ, is explained by the underlying structure of constituting fermionic spinons. Our calculation demonstrates that the Gutzwiller projection does not necessarily broaden the spectrum in $\boldsymbol{k}$ space. As shown in Fig. 8(b), this phenomenology is not necessarily related to the presence of strings in the trial state: it can also be observed for shorter strings when $t < J$.

The situation described above, with a single hole moving in an SU(2)-invariant spin background $B_{st} = 0$, is directly relevant to the magnetic polaron problem in the J_1-J_2 model on a square lattice. Upon increasing the frustrating diagonal next-nearest-neighbor coupling J_2, the staggered magnetization in the undoped system approaches zero [95], corresponding to the choice $B_{st} \to 0$ in the variational wave function. We expect that the spinon-chargon trial wave function can be used to describe a single mobile hole in the frustrated J_1-J_2 background, as long as the tunneling rate dominates $t \gg J_{1,2}$, and strong local AFM correlations are present.

III. DISCUSSION AND OUTLOOK

In this paper, we discussed a microscopic parton theory of ARPES spectra in 2D quantum AFMs. At strong couplings, where the tunneling rate t dominates over spin-exchange terms J, the geometric string approach [35,47,66] allows us to approximate the spinon-chargon wave function as product state of Born-Oppenheimer type. We showed that this results in an ARPES spectrum which can be written as a convolution of a spinon and a chargon (or string) contribution. When the spinon and chargon form a bound state, the chargon contribution provides a $\boldsymbol{k}$-independent overall renormalization Z_c, whereas the spinon contribution $Z_s(\boldsymbol{k})$ is strongly $\boldsymbol{k}$ dependent in general. Conversely, only $Z_c(t/J)$ depends on the ratio t/J, reflecting the size of the spinon-chargon bound state, whereas the spinon contribution Z_s is independent of the tunneling amplitude t.

We demonstrated that the ARPES spectrum of a single hole in the 2D t-J model, characterizing the structure of magnetic polarons, can be described by the parton theory. In particular, we established that the spinon part of the quasiparticle weight $Z_s = Z/Z_c$ becomes only weakly dependent on t/J in the strong coupling limit $t \gg J$ where our theory is valid; $Z_c(t/J)$ can be calculated from a semianalytical string-based calculation. Using td-MPS simulations [61,93], we calculated the momentum dependence of the spectral weight $A(\omega, \boldsymbol{k})$, which is strongly suppressed over a wide energy range around $\boldsymbol{k} = (\pi,\pi)$. Using the parton theory, we argued that this suppression can be understood as a signature of fermionic spinon statistics. We supported this conclusion by showing that all qualitative features of $Z(\boldsymbol{k})$ can be reproduced by a

spinon-chargon trial wave function based on fermionic constituting spinons and including stringlike spin-charge correlations [35].

We obtained even more direct signatures for the formation of fermionic spinons for a doped Dirac spin liquid. Across the location of the spinon Dirac cone in the Brillouin zone, we predict a sharp drop of the quasiparticle weight using our trial wave function. We explained this feature by a mean-field theory based on constituting fermionic spinons, whose quasiparticle residue changes abruptly across the Dirac cone at the nodal point.

Our work establishes a possible link to the Fermi arcs observed in the pseudogap phase of cuprates. We speculate that our observation that the spectral weight is strongly suppressed up to high energies around $\boldsymbol{k} = (\pi, \pi)$ may be a precursor of the missing spectral weight outside the MBZ in the context of Fermi arcs. We identified two important ingredients required for this phenomenology: (i) strong couplings $t \gg J$, leading to extended geometric strings, and (ii) sufficient frustration, leading to a small AFM order parameter. In the cuprate compounds, typical values of t/J are around 3, well within the strong coupling regime. Next, we will argue that the required kind of frustration is naturally introduced by the mobile dopants themselves in the pseudogap regime.

A. Parton theory at finite doping

The parton theory can be easily extended to finite but small doping, if we assume that correlations between the chargons can be neglected and they remain bound to individual spinons by geometric strings. Experimental studies in ultracold-atom systems suggest that these conditions may be justified up to a maximum doping level of about 15% [46,47]. Beyond this regime, magnetic polarons begin to overlap, and interactions can modify our picture significantly. In the following, we focus on the low-doping case.

As long as the geometric string picture can be applied, the dispersion of magnetic polarons is dominated by the spinon properties. The number of spinons $N_s = L^2(1 - n_h)$ decreases with increasing hole doping n_h, and on the mean-field level the spinon Fermi sea, or band insulator for $B_{st} \neq 0$, is below half-filling. Hence, fewer states contribute to the ARPES spectrum, and at the lowest energy we expect to see the spinon Fermi surface.

The variational parameters B_{st}/J_{eff} and Φ of the mean-field spinon Hamiltonian (14) are expected to depend on the doping level n_h. For $n_h = 0$ the optimal parameters correspond to the half-filled Heisenberg model [45], which we used in this paper. At finite doping $n_h > 0$, in contrast, the geometric strings introduce effective next-nearest-neighbor (and further) interactions $J_2(n_h)$ in the spin background $|\Psi\rangle$ used to define the FSA product wave function (5): in a state $|\Sigma\rangle = \hat{G}_\Sigma|\Psi\rangle$, the spins along the geometric string Σ are displaced by one site. The instantaneous spin-exchange coupling $\hat{\mathcal{H}}_J$ in state $|\Sigma\rangle$ hence includes interactions between spins that used to be next-nearest neighbors in the original state $|\Psi_0\rangle$. Averaging over all string configurations Σ contributing to the spinon-chargon bound states thus leads to the estimate

$$J_2(n_h) \simeq J n_h \bar{\ell}_\Sigma, \tag{20}$$

where $\bar{\ell}_\Sigma$ is the average length of geometric strings. By the same argument, nearest-neighbor interactions J_1 are effectively reduced: $J_1(n_h) = J(1 - n_h\bar{\ell}_\Sigma)$.

As discussed earlier, the presence of frustrating next-nearest-neighbor (and further-range) couplings $J_2(n_h)$ leads to reduced AFM order B_{st} in the mean-field spinon Hamiltonian [95]. Finite temperature is expected to have a similar effect. Once $B_{st} = 0$, the trial wave function no longer breaks the discrete translational symmetry of the square lattice. In this case, the spinons can still form a small Fermi surface, and we speculate that the spinon-chargon pairs could form a fractionalized Fermi-liquid state [80,81]. From our insights obtained for a single dopant, we expect that the backside of the corresponding spinon Fermi surface would be invisible in the spectral function, as a consequence of the formation of gapless Dirac cones at the nodal points in the spinon dispersion. The mean-field theory further predicts that the spectral weight smoothly vanishes as one encircles the nodal point [see Fig. 6(c)]. This phenomenology is in agreement with the experimental findings [39].

Another interesting extension of our work in the context of the dimensional crossover concerns the relation of the spinon-chargon picture to antiholons observed in the supersymmetric 1D t-J model at $J = 2t$ [107].

B. Probing frustrated quantum magnets

Beyond the t-J and, by extension, the Fermi-Hubbard model, our results are also relevant to other strongly correlated quantum spin systems. Our main assumptions within the geometric string approach are (i) that we work in the strong coupling regime, where the tunneling t dominates over spin-exchange terms, and (ii) that the string basis used for the formulation of the FSA wave function in Eq. (5) is valid. We expect that (ii) can be satisfied, provided that the system has sufficiently strong *local* AFM correlations.

Under these assumptions, our microscopic parton theory describes general quantum AFMs. According to our results, the corresponding ARPES spectrum should directly reveal the properties of the constituting spinons, including the shape of their dispersion relation and the distribution of spectral weight. Such studies are similar to calculations of the dynamical spin-structure factor (see, e.g., Refs. [64,65,95]), but as a main advantage they involve one instead of two spinons. This approach may prove to be particularly useful to reveal the nature of quantum spin liquids with deconfined spinon excitations. Concrete examples may include studies of the frustrated Heisenberg model on a kagome lattice [108], where it remains debated wether the ground state is gapped $\mathbb{Z}_2$ or a gapless Dirac spin liquid, or the J_1-J_2 model on a triangular lattice where new signatures of Dirac spin liquids have recently been reported [109]. Exact diagonalization studies of the one-hole ARPES spectra for small kagome systems have already been performed [106]. Our studies are of particular interest in light of the recent proposal that U(1) Dirac spin liquids may provide a unified starting point for describing a range of 2D quantum magnets on different lattices [85].

C. Experimental considerations

ARPES is a standard tool in solid state physics, and has been used extensively to study strongly correlated quantum

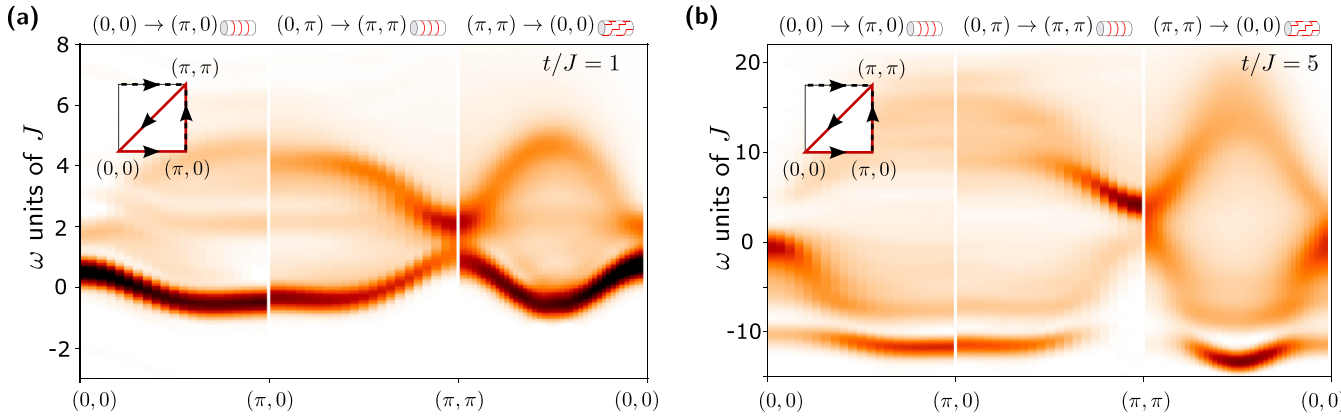

FIG. 9. One-hole spectral function. As in Fig. 1 of the main text, we use td-MPS methods to calculate the single-hole spectrum in the t-J model on a 4×40 cylinder. In (a) we used $t/J = 1$ and in (b) we set $t/J = 5$.

matter such as the cuprate compounds [1]. The presence of phonons makes a direct comparison of experimental ARPES spectra and theoretical calculations for the simplified t-J model challenging [36,37]. However, the rapid progress of quantum simulation experiments with ultracold atoms has recently enabled experiments in clean model systems with tunable parameters, where ARPES measurements can also be performed [55–60]. In particular, the 2D Fermi Hubbard model can be studied and long-standing questions about strongly correlated quantum matter can now be addressed. Ultracold polar molecules allow for a direct implementation of t-J models [110].

In optical lattices, the lowest temperatures have been achieved in quantum gas microscopy setups so far [52], which can also be used to measure the spectral function [59,60]. Experiments implementing triangular lattices are currently under construction, paving the way for spectroscopic studies of highly frustrated quantum magnets in the near future. Other applications include systematic investigations of the dimensional crossover, which we studied in this paper, or studies of ARPES spectra in bilayer systems.

ACKNOWLEDGMENTS

The authors thank Z. X. Shen, Z. Zhu, S. Sachdev, A. Vishwanath, T. Giamarchi, U. Schollwöck, C. Hubig, I. Cirac, R. Verresen, D. Chowdhury, M. Punk, Y. Wang, A. Rosch, I. Bloch, M. Endres, G. Salomon, D. Greif, W. Bakr, and P. Schauss for fruitful discussions. We additionally want to thank R. Verresen for sharing parts of the numerical code. We acknowledge support from the Technical University of Munich–Institute for Advanced Study, funded by the German Excellence Initiative and the European Union FP7 under Grant Agreement No. 291763, the Deutsche Forschungsgemeinschaft (DFG, German Research Foundation) under Germanys Excellence Strategy-EXC-2111-390814868, DFG TRR80 and DFG Grant No. KN1254/1-1, and from the European Research Council (ERC) under the European Unions Horizon2020 research and innovation programme (Grant Agreement No. 851161). We acknowledge support from the Studienstiftung des deutschen Volkes, Harvard-MIT CUA, AFOSR-MURI: Photonic Quantum Matter (Award No. FA95501610323), DARPA DRINQS program (Award No. D18AC00014). F.P. acknowledges support by the European Research Council (ERC) under the European Unions Horizon 2020 research and innovation program (Grant Agreement No. 771537), the DFG Research Unit FOR 1807 through Grants No. PO 1370/2- 1 and No. TRR80, and the Deutsche Forschungsgemeinschaft (DFG, German Research Foundation) under Germanys Excellence Strategy EXC-2111-390814868.

APPENDIX A: td-MPS SIMULATIONS AND DMRG

In Fig. 9 we present more numerical results for the ARPES spectrum for different values of t/J.

1. Calculating the spectral function

The spectral function is calculated as the Fourier transform of the time-dependent correlation function

$$C_{\mathbf{i},\mathbf{j}}(t) = \sum_{\sigma} \langle \psi_0 | e^{i\hat{H}t} \hat{c}^{\dagger}_{\mathbf{j},\sigma} e^{-i\hat{H}t} \hat{c}_{\mathbf{i},\sigma} | \psi_0 \rangle. \tag{A1}$$

Here, $|\psi_0\rangle$ is the ground state of the t-J model without a hole, i.e., the Heisenberg model, on a cylinder with four legs. The time evolution of the ground state with the t-J Hamiltonian $e^{i\hat{H}t}|\psi_0\rangle = e^{iE_0 t}|\psi_0\rangle$. We thus calculate the following:

(i) the ground state without a hole $|\psi_0\rangle$, using DMRG;

(ii) the time evolution of the ground state after a hole was created in the origin $|\psi(t)\rangle = e^{-i\hat{H}t}\hat{c}_{\mathbf{0},\sigma}|\psi_0\rangle$;

(iii) the overlap of $|\psi(t)\rangle$ with the state where a hole was created at a position $\mathbf{j}$, $|\psi_1\rangle = \hat{c}_{\mathbf{j},\sigma}|\psi_0\rangle$.

The time evolution of $\hat{c}_{\mathbf{0},\sigma}|\psi_0\rangle$ is performed using the matrix product operator based time evolution introduced in Ref. [61]; see also Refs. [62–65].

In Fig. 10 we compare the correlation function $C_{\mathbf{i},\mathbf{j}}(t)$ for different bond dimensions χ at a time of $t_0 = 8\ (1/J)$, which is the maximal time used for our calculation of the spectral function shown in the main text. While there are small differences in the absolute numbers, the qualitative behavior is captured correctly already at a bond dimension of $\chi = 600$. For later times, the deviations between different bond dimensions increase further.

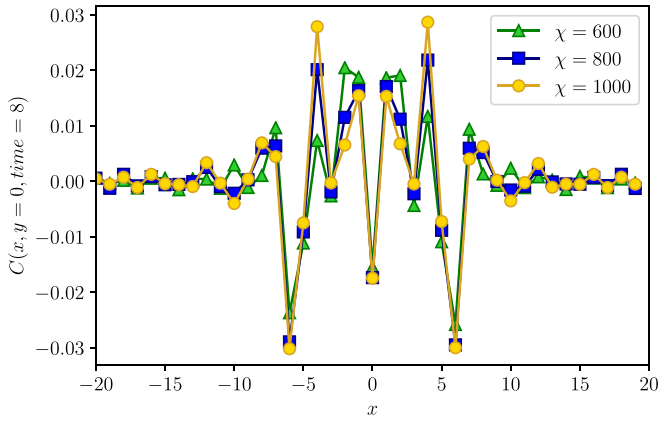

FIG. 10. Convergence of td-MPS data. We check the convergence of our td-MPS calculations with the bond dimension χ in the real time and space correlation function $C_{\mathbf{i},\mathbf{j}}(t)$ for the latest time (8 in units of $1/J$) considered for $t/J = 3$.

We perform a spatial Fourier transform to obtain

$$A(\mathbf{k}, t) = \sum_{\mathbf{j}} e^{-i\mathbf{k}\cdot\mathbf{j}} C_{\mathbf{0},\mathbf{j}}(t). \tag{A2}$$

As our time evolution is limited to times $0 \leqslant t \leqslant t_0 = 8/J$, we use linear prediction to increase the time window. Afterward, the data are multiplied with a Gaussian envelope $w(t) = \exp[-0.5(t\sigma_\omega)^2]$, where $\sigma_\omega = 2/t_0 = 0.25J$ is chosen in order to minimize the weight of the data generated by linear prediction in the spectrum [65]. An example of a time trace used for our calculation of the spectral function is shown in Fig. 11. We confirmed that the results do not depend on the details of this procedure. Fourier transforming in time yields the spectral function

$$A(\mathbf{k}, \omega) = \frac{1}{2\pi} \int_{-\infty}^{\infty} dt A(\mathbf{k}, t). \tag{A3}$$

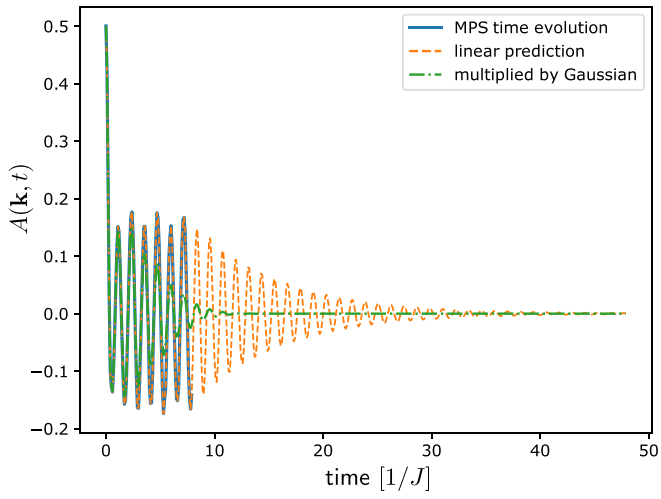

FIG. 11. Linear prediction and Gaussian envelope. After the spatial Fourier transform, we use linear prediction to enhance the time window (orange dashed). Before Fourier transforming in time, the time-dependent data are multiplied with a Gaussian envelope of width $\sigma_\omega = 0.25J$ (green dashed-dotted). Here, as an example, we show the corresponding time traces for $k_x = 0$, $k_y = \pi/2$ at $t/J = 3$.

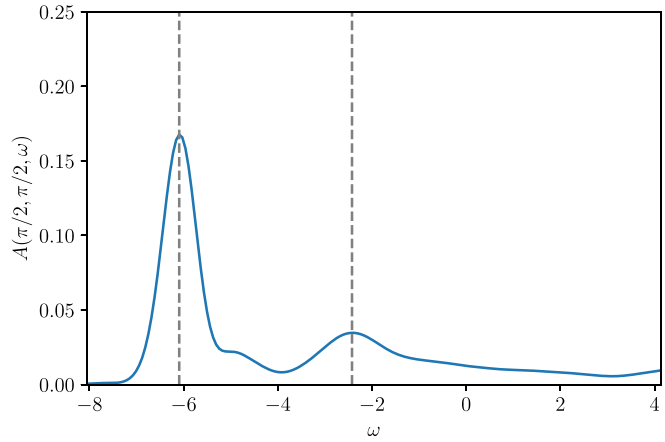

FIG. 12. First vibrational peak. We show the frequency cut of the one-hole spectral function at the nodal point $\boldsymbol{k} = (\pi/2, \pi/2)$, for the same parameters as in Fig. 1(a) of the main text. The extracted positions of the ground state (first peak) and vibrationally excited (second peak) magnetic polaron are indicated by dashed lines.

In this signal, the Gaussian envelopes introduced in the time domain before lead to Gaussian broadening of the obtained peaks, sufficiently small for our analysis.

The diagonal cut through the Brillouin zone from (0,0) to (π, π) is obtained by labeling the sites around the cylinder in a *zigzag* fashion as indicated in the top row of Fig. 1(a). One ring around the cylinder with this labeling contains $2L_r$ instead of L_r sites, where L_r is the circumference of the cylinder. We calculate the ground state as well as the dynamics with the couplings in the Hamiltonian according to this modified lattice geometry used for representing the MPS. For each time step, we obtain an array with $L_x \times 2L_r$ entries, where L_x is the length of the cylinder. This array is reshaped into an $2L_x \times L_r$ array and then the Fourier transform is performed, yielding $A(\mathbf{k}, t)$. Due to the relabeling of the sites, the momenta are transformed as

$$\begin{aligned} k_x &\to k_x, \\ k_y &\to k_y + k_x. \end{aligned} \tag{A4}$$

In particular, for $k_y = 0$ we obtain the cut from (0,0) to (π, π) shown in the rightmost panel of Fig. 1(a).

2. Extracting peak positions and quasiparticle weight

From cuts at fixed momenta $\mathbf{k}$, the positions of the low energy peaks visible in Fig. 1(a) can be extracted. Figure 12 shows the corresponding cut at momentum $\mathbf{k} = (\pi/2, \pi/2)$ for $t/J = 3$.

It can be shown analytically that the ground-state quasiparticle weight $Z(\pi/2, \pi/2)$ shown in Fig. 3 in the main text corresponds to the integral over the first peak in the spectral function. However, $Z(\pi/2, \pi/2)$ can be expressed more conveniently as the overlap:

$$Z(\pi/2, \pi/2) = \sum_{\sigma} \left| \langle \psi_0^{1\mathrm{h}} | \hat{c}_{(\pi/2,\pi/2),\sigma} | \psi_0^{0\mathrm{h}} \rangle \right|^2. \tag{A5}$$

We can thus obtain the quasiparticle weight directly from the ground states of the t-J model without a hole, $|\psi_0^{0\mathrm{h}}\rangle$, and with a single hole, $|\psi_0^{1\mathrm{h}}\rangle$, without the need to calculate any time

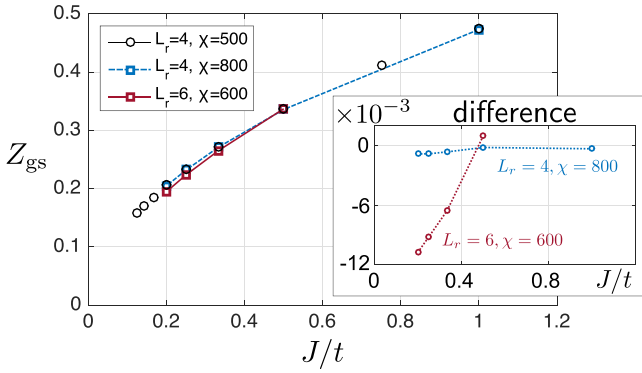

FIG. 13. Dependence of DMRG data on parameters. We check how our DMRG calculations of the ground-state quasiparticle weight Z change when the bond dimension χ and the circumference L_r of the cylinder are changed. The inset shows the difference $Z_{gs}(L_r, \chi) - Z_{gs}(L_r = 4, \chi = 500)$; note the overall scale 10^{-3}.

evolution. The ground state of a single hole in the t-J model has momentum $\mathbf{k} = (\pi/2, \pi/2)$. In a translational-invariant system, we can further simplify the calculation by writing

$$Z(\pi/2, \pi/2) = \sum_{\sigma} \sum_{j} \left| \langle \psi_0^{1h} | \hat{c}_{j,\sigma} | \psi_0^{0h} \rangle \right|^2. \tag{A6}$$

Hence, we only need to calculate the overlap of the one-hole ground state with a locally created hole at different positions $\boldsymbol{j}$: $\hat{c}_{j,\sigma}|\psi_0^{0h}\rangle$. In Fig. 13 we show how this procedure changes with the bond dimension χ and circumferences $L_r = 4$ and 6, for different t/J.

A comment is in order concerning the use of Eq. (A6). To employ it in our finite-size cylinders, we must assume that the ground state $|\psi_0^h\rangle$ does not spontaneously break the translational symmetry in the thermodynamic limit and can be well approximated by a standing wave of nodal point momenta $\pm(\pi/2, \pm\pi/2)$ in the finite-size system. In Refs. [111,112] Zhu *et al.* have shown in few-leg ladders with open boundary conditions that the finite-size ground state $|\psi_0^h\rangle$ can show manifestations of a spontaneously broken translational symmetry in the thermodynamic limit, as indicated by strong charge modulations in the finite-size ground state. In our numerics on four-leg cylinders, we find no indications for this scenario.

To extract $Z(\boldsymbol{k})$ for $\boldsymbol{k}$ different from the nodal points, we determine the height of the first peak and its full width at half-maximum. We assume a Gaussian form and thus calculate $Z(\boldsymbol{k})$ as the corresponding integral over the Gaussian function.

APPENDIX B: FSA ANSATZ

We calculate the chargon, or string, contribution to the quasiparticle weight $Z_c(J/t)$ using the FSA ansatz from Eq. (5) in the main text, assuming that geometric string states are mutually orthogonal, $\langle \Sigma | \Sigma' \rangle \approx \delta_{\Sigma,\Sigma'}$. In addition, we simplify the effective string Hamiltonian [see Fig. 14(a)]

$$\hat{\mathcal{H}}_\Sigma = -t \sum_{\langle \Sigma', \Sigma \rangle} (|\Sigma'\rangle\langle\Sigma| + \text{H.c.}) + \sum_{\Sigma} V_{\text{pot}}(\Sigma) |\Sigma\rangle\langle\Sigma| \tag{B1}$$

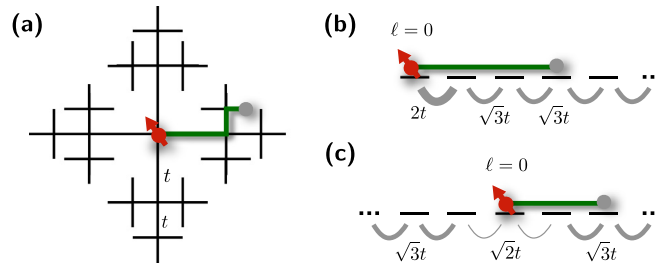

FIG. 14. Spinon-chargon repulsion. (a) We consider a model where the charge fluctuations are described by string states, corresponding to the sites of a Bethe lattice. (b) Assuming a central-symmetric potential on the Bethe lattice, the one-particle hopping problem on the Bethe lattice, describing the fluctuating string, can be mapped to a semi-infinite one-dimensional chain with the indicated hopping amplitudes and a linear potential along the chain. (c) The problem in (b) can be related to an infinite one-dimensional problem with a mirror symmetry around the origin and *reduced* hopping matrix elements $\sqrt{2}t$ to the central site, as compared to $\sqrt{3}t$ elsewhere. As described in the text, this inhomogeneous tunneling gives rise to a strong (of order t) microscopic spinon-chargon repulsion.

by making the linear string approximation [35]

$$V_{\text{pot}}(\Sigma) \approx V_{\text{LST}}(\ell_\Sigma) = \frac{dE}{d\ell} \ell_\Sigma + g_0 \delta_{\ell_\Sigma,0} + \mu_h. \tag{B2}$$

Here, ℓ_Σ denotes the length of string Σ and the linear string tension is given by $dE/d\ell = 2J(C_2 - C_1)$, where C_2 (C_1) is the diagonal next-nearest-neighbor (nearest-neighbor) spin correlator $\langle \hat{\boldsymbol{S}}_i \cdot \hat{\boldsymbol{S}}_j \rangle$ in the undoped Heisenberg AFM. The additional pointlike spinon-chargon attraction is given by $g_0 = -J(C_3 - C_1)$ with C_3 the next-next-nearest neighbor correlator. The zero-point energy $\mu_h = J(1 + C_3 - 5C_1)$ provides an overall energy offset; see Ref. [35] for more details.

Equation (B1) describes a hopping problem on a Bethe lattice in the presence of a central-symmetric potential. Making use of all discrete rotational symmetries at the branches of the Bethe lattice, the problem can be reduced to a single particle in an effective semi-infinite one-dimensional lattice [66,71] [see Fig. 14(b)]:

$$\hat{\mathcal{H}}_{\text{eff}} = \left[-2t|1\rangle\langle 0| - \sqrt{3}t \sum_{\ell=1}^{\infty} |\ell+1\rangle\langle\ell| + \text{H.c.} \right] + \sum_{\ell=0}^{\infty} V_{\text{LST}}(\ell) |\ell\rangle\langle\ell|, \tag{B3}$$

which can be solved exactly numerically. From the solution $|\psi_\Sigma\rangle = \sum_{\ell=0}^{\infty} \psi_\ell |\ell\rangle$, we obtain the chargon contribution to the quasiparticle weight as $Z_c = |\psi_{\ell=0}|^2$. This result is plotted in Fig. 3 of the main text. By diagonalization of Eq. (B3) the excitation energy of the first vibrational state is also obtained, which we plot in Fig. 2 as a function of t/J.

Now, we discuss how $Z_c(J/t)$ depends on J/t, focusing in particular on the asymptotic behavior when $J/t \to 0$. A naive mapping of Eq. (B3) to the continuum limit $\ell \in \mathbb{R}_{>0}$ yields the Schrödinger equation [71]

$$\left[-\sqrt{3}t\, \partial_\ell^2 + \frac{dE}{d\ell} \ell - E \right] \psi(\ell) = 0. \tag{B4}$$

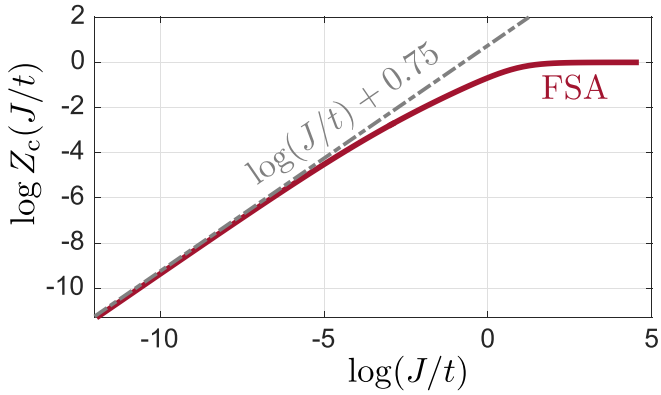

FIG. 15. Chargon contribution the quasiparticle weight. $Z_c(J/t)$ is calculated from the model in Eq. (B3), based on the frozen spin approximation (FSA), and shown in a double-logarithmic plot. In the strong coupling regime $J \ll t$ the asymptotic power law $Z_c(J/t) \propto J/t$ is obtained as a result of spinon-chargon repulsion.

It is well known that the competition of the kinetic energy $\propto t$ and the linear string tension $dE/d\ell \propto J$ leads to an emergent average string length $L_\Sigma \propto (t/J)^{1/3}$ [71]. Hence, one would naively expect $Z_c = |\psi_{\ell=0}|^2 \simeq L_\Sigma^{-1} = (J/t)^{1/3}$. When $J \simeq t$ are comparable in magnitude, such behavior is indeed observed [26]. For most values shown in Fig. 3 the residue of the magnetic polaron $Z(J/t) \simeq (J/t)^\alpha$ can be approximated by a power law, and for $t \simeq J$ the exponent $\alpha < 1$ is significantly below one. This is consistent with the naive expectations above.

In Fig. 15 we calculate $Z_c(J/t)$ from the model in Eq. (B3) and show the result in a log-log plot. For $J \ll t$, in the strong coupling regime, our result demonstrates that $Z_c(J/t) \simeq J/t$, i.e. asymptotically the exponent of the power law approaches $\alpha = 1$. This indicates that additional spinon-chargon repulsion must be present in the effective continuum model (B4), which enhances the exponent from $\alpha = \frac{1}{3}$ to 1 at strong couplings.

The origin of additional spinon-chargon repulsion can be understood by mapping the semi-infinite one-dimensional problem (B3) to the even-parity sector of the following infinite problem [see Fig. 14(c)]:

$$\hat{\mathcal{H}}'_{\rm eff} = -\sqrt{3}t \sum_{\ell=-\infty}^{\infty} [(1-\delta_{\ell,0}-\delta_{\ell,-1})|\ell+1\rangle\langle\ell| + \text{H.c.}]$$
$$- \sqrt{2}t[|1\rangle\langle 0| + |0\rangle\langle -1| + \text{H.c.}] + \sum_{\ell=-\infty}^{\infty} V_{\rm LST}(\ell)|\ell\rangle\langle\ell|. \tag{B5}$$

One can confirm that every even-parity eigenstate $\phi_{-\ell} = \phi_\ell$ of $\hat{\mathcal{H}}'_{\rm eff}$ corresponds to an eigenstate of $\hat{\mathcal{H}}_{\rm eff}$ given by $\psi_\ell = \sqrt{2}\phi_\ell$ for $\ell > 0$ and $\psi_{\ell=0} = \phi_{\ell=0}$, with the same eigenenergy.

Equation (B5) describes a single particle hopping in an infinite chain in the presence of a central-symmetric confining potential. Around the origin, the tunneling amplitudes are reduced from $\sqrt{3}t$ in the bulk to $\sqrt{2}t$. This reduces the zero-point kinetic energy from $-2\sqrt{3}t$ in the bulk to $-2\sqrt{2}t$ in the origin, corresponding to a localized repulsive potential with a strength of the order $2(\sqrt{3}-\sqrt{2})t = 0.64t$. At strong couplings this repulsion overcomes the spinon-chargon attraction $\propto g_0 \propto J$ included in $V_{\rm LST}(\ell)$ [see Eq. (B2)], and leads to the formation of a node at $\ell = 0$ in the string wave function when $J \ll t$. This effect is not included in the naive continuum theory (B4), and explains why we observe $Z_c(J/t) \propto J/t$ asymptotically when $J/t \to 0$.

The effective local spinon-chargon repulsion $\propto t$ is determined by the connectivity of the Bethe lattice defining the string basis. For chargons moving only along one dimension, as realized for example in the mixed-dimensional t-J model [83], this additional repulsion is absent. In such settings, a different power law is reached asymptotically at strong couplings.

APPENDIX C: SPINON-CHARGON TRIAL WAVE FUNCTION

We use the trial wave function from Eq. (12) to calculate the quasiparticle weight $Z(\boldsymbol{k})$ [see Eq. (15)]. To evaluate the expression in Eq. (15) we use Metropolis Monte Carlo.

1. Sampling

We sample Fock configurations $|\alpha\rangle$ of the fermionic spinons $\hat{f}_{j,\sigma}$, and two sets of string configurations Σ and Σ' from the following positive-definite distribution:

$$\rho_J(\alpha, \Sigma, \Sigma') = |\psi_\Sigma||\psi_{\Sigma'}||\langle\Psi_{\rm MF}(\boldsymbol{k},\sigma)|\alpha_\Sigma\rangle| \times |\langle\Psi_{\rm MF}(\boldsymbol{k},\sigma)|\alpha_{\Sigma'}\rangle|. \tag{C1}$$

Here, $|\Psi_{\rm MF}(\boldsymbol{k},\sigma)\rangle = \hat{f}^\dagger_{\boldsymbol{k},\sigma,-}|\Psi^{\rm SF+N}_{\rm MF}\rangle$ is the mean-field state with one extra spinon excitation of momentum $\boldsymbol{k}$ in the lower spinon band ($\mu = -$). We further introduced the squeezed-space Fock configurations

$$|\alpha_\Sigma\rangle = \hat{G}^\dagger_\Sigma|\alpha\rangle, \tag{C2}$$

where the operator $\hat{G}_\Sigma$ also appears in the definition of the trial wave function (12) and creates a state with a geometric string Σ starting at the position of the hole in the Fock state to its right; see Eq. (4).

To calculate $Z(\boldsymbol{k})$ we introduce a completeness relation of one-hole Fock states $\sum_\alpha |\alpha\rangle\langle\alpha| = \hat{1}_{\rm 1h}$, and use momentum conservation. This leads to

$$Z(\boldsymbol{k}) = \frac{1}{\sqrt{\mathcal{N}_0\mathcal{N}_1}} \sum_\sigma \sum_j \frac{e^{i\boldsymbol{k}\cdot\boldsymbol{j}}}{L} \sum_\Sigma \psi^*_\Sigma \sum_\alpha \times \langle\Psi_{\rm MF}(\boldsymbol{k},\sigma)|\hat{\mathcal{P}}_{\rm GW}|\alpha_\Sigma\rangle\langle\alpha|\hat{f}_{j,\sigma}\hat{\mathcal{P}}_{\rm GW}|\Psi^{\rm SF+N}_{\rm MF}\rangle, \tag{C3}$$

with the normalizations

$$\mathcal{N}_0 = \langle\Psi_{\rm sc}(\boldsymbol{k})|\Psi_{\rm sc}(\boldsymbol{k})\rangle, \tag{C4}$$
$$\mathcal{N}_1 = \langle\Psi^{\rm SF+N}_{\rm MF}(\boldsymbol{k})|\hat{\mathcal{P}}_{\rm GW}|\Psi^{\rm SF+N}_{\rm MF}(\boldsymbol{k})\rangle. \tag{C5}$$

Note that for the trial wave function it holds $|\Psi_{\rm sc}(\boldsymbol{k})\rangle \equiv |\Psi_{\rm sc}(\boldsymbol{k}+\boldsymbol{K})\rangle$ for reciprocal lattice vectors $\boldsymbol{K}$.

The first Gutzwiller projection in Eq. (C3) can be dropped since it acts on a Fock configuration to the right. The second Gutzwiller projection can be handled in a similar way, by writing

$$\frac{1}{L}\sum_j e^{-i\boldsymbol{k}\cdot\boldsymbol{j}}\hat{\mathcal{P}}_{\rm GW}\hat{f}^\dagger_{j,\sigma}|\alpha\rangle = \frac{L^2/2}{L}e^{-i\boldsymbol{k}\cdot\boldsymbol{j}^{\rm h}_\alpha}|\tilde{\alpha}\rangle, \tag{C6}$$

where $L^2/2|\tilde{\alpha}\rangle = \hat{\mathcal{P}}_{\rm GW}\hat{f}^\dagger_{\boldsymbol{j},\sigma}|\alpha\rangle$ and $\boldsymbol{j}^{\rm h}_\alpha$ denotes the position of the hole in the Fock configuration $|\alpha\rangle$. The state $|\tilde{\alpha}\rangle$ is thus obtained from $|\alpha\rangle$ by adding a fermion at site $\boldsymbol{j}^{\rm h}_\alpha$. The extra factor $L^2/2 = N_\sigma$ is equal to the number of spins σ in Fock state $|\alpha\rangle$, and arises when relating the properly normalized first ($|\tilde{\alpha}\rangle$) and second ($\hat{\mathcal{P}}_{\rm GW}\hat{f}^\dagger_{\boldsymbol{j},\sigma}|\alpha\rangle$) quantized many-body states.

Combining the results above, we can write $Z(\boldsymbol{k})$ as

$$Z(\boldsymbol{k}) = \sum_\sigma \sum_{\Sigma,\Sigma'} \sum_\alpha \rho_J(\alpha,\Sigma,\Sigma') \frac{\delta_{\Sigma,\Sigma'}\, \psi^*_\Sigma \,\langle \Psi_{\rm MF}(\boldsymbol{k},\sigma)|\alpha_\Sigma\rangle\, e^{i\boldsymbol{k}\cdot\boldsymbol{j}^{\rm h}_\alpha} \langle \tilde{\alpha}|\Psi^{\rm SF+N}_{\rm MF}\rangle}{\rho_J(\alpha,\Sigma,\Sigma')\sqrt{2}} \mathcal{N}^{-1/2}, \tag{C7}$$

where

$$\mathcal{N} = \left[\sum_{\Sigma,\Sigma'}\sum_\alpha \rho_J(\alpha,\Sigma,\Sigma') \frac{\psi^*_\Sigma\,\psi_{\Sigma'}\,\langle\Psi_{\rm MF}(\boldsymbol{k},\sigma)|\alpha_\Sigma\rangle\,\langle\alpha_{\Sigma'}|\Psi_{\rm MF}(\boldsymbol{k},\sigma)\rangle}{\rho_J(\alpha,\Sigma,\Sigma')}\right]\left[\sum_{\Sigma,\Sigma'}\sum_\alpha \rho_J(\alpha,\Sigma,\Sigma') \frac{\delta_{\Sigma,\Sigma'}\,|\psi_\Sigma|^2\,\left|\langle\Psi^{\rm SF+N}_{\rm MF}|\tilde{\alpha}_\Sigma\rangle\right|^2}{\rho_J(\alpha,\Sigma,\Sigma')}\right]. \tag{C8}$$

This is the expression we used to perform a Metropolis Monte Carlo procedure, sampling from the distribution $\rho_J(\alpha,\Sigma,\Sigma')$. Note that the required Fock-state overlaps can be straightforwardly evaluated (see, e.g., [45,101]).

2. Parameter dependence

We worked with Eq. (C7) to check how the quasiparticle residue of the trial wave function depends on various parameters. In Fig. 16 we compare $Z(\boldsymbol{k})$ along a diagonal cut through the magnetic Brillouin zone for different system sizes. While the smallest 4×4 torus shows strong finite-size effects, already the results for 6×6 and 4×10 tori agree within error bars. We show that the result does not change significantly when increasing the system size further, up to 12×12 and 20×20, indicating that finite-size scaling of our results obtained in 12×12 systems is not necessary.

In Fig. 17(a) we show how $Z(\boldsymbol{k})$ depends on the linear string tension, which determines how tightly the chargon is bound to the spinon. We rescaled the FSA expression for $dE/d\ell$, introduced below Eq. (B2), by a factor $\lambda_{dE/d\ell}$. The data shown in the main text correspond to $\lambda_{dE/d\ell} = 1$. Assuming tighter spinon-chargon confinement leads to significantly increased spectral weight. This may explain why the result by the trial wave function in Fig. 3 of the main text showed too small quasiparticle residues as compared to the numerically obtained results starting from first principles. Note that similar indications for tighter spinon-chargon confinement have been obtained in studies of the variational energy [35].

In Fig. 17(b) we show how $Z(\boldsymbol{k})$ depends on the staggered field $B_{\rm st}/J_{\rm eff}$ characterizing the undoped trial wave function. In the limit $B_{\rm st}/J_{\rm eff}\to 0$ different behavior is observed for momenta $\boldsymbol{k}$ within and outside the magnetic Brillouin zone. For larger values of $B_{\rm st}/J_{\rm eff}$, larger quasiparticle residues are obtained. This may also play a role for explaining the deviations observed in Fig. 3 of the main text between the trial wave function and numerical approaches.

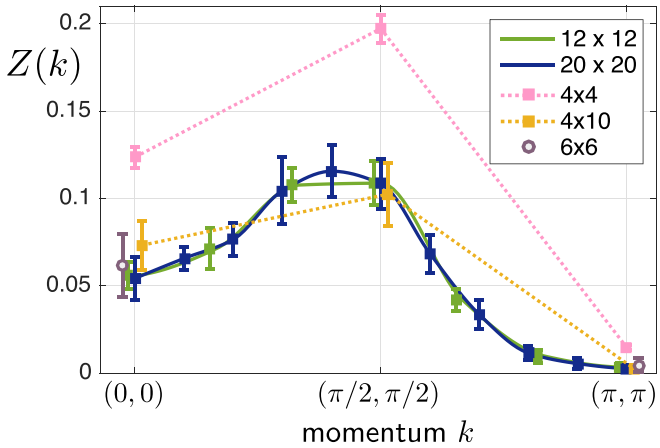

FIG. 16. Size dependence of the quasiparticle weight. $Z(k)$ is shown along the diagonal cut from (0,0) to (π,π). We evaluated the spinon-chargon trial wave function for different system sizes (see legend). No significant finite-size dependence can be observed beyond 6×6. We set $t/J = 3$, $B_{\rm st}/J_{\rm eff} = 0.44$, and $\Phi = 0.4\pi$. Solid lines are guides to the eye only. Some data points are slightly offset horizontally for better visibility; for 6×6 only a selection of $\boldsymbol{k}$ points are shown.

APPENDIX D: DISCUSSION OF FINITE-SIZE EFFECTS

In this Appendix, we summarize to which extent our td-MPS and DMRG data on four- and six-leg cylinders can be considered as reliable approximations of the genuine 2D t-J model.

The first indicator we consider concerns the entire spectrum: Due to the fourfold discrete rotational symmetry of the genuine 2D model, momenta $(0,\pi)$ and $(\pi,0)$ must have identical ARPES spectra. This symmetry is broken on the 4×40 cylinders we consider, and indeed the spectra at $(0,\pi)$ and $(\pi,0)$ are not exactly identical in our Figs. 1 and 9 (note the actual cuts indicated on the top of all spectra). However, we find perfect qualitative agreement of the spectra at $(0,\pi)$ and $(\pi,0)$ as expected, and only relatively small quantitative deviations, indicating that finite-size effects are relatively weak at all energies and for different ratios t/J.

The second indicator we consider concerns only the ground state, for which we compare the quasiparticle weights Z. We start by the finite-size analysis based on our trial wave function, at $t/J = 3$. Figure 16 shows that strong finite-size effects persist for the 4×4 torus, in agreement with the significant finite-size effects observed in 4×4 systems using exact diagonalization [26]. Already for the 6×6 system, our trial wave function predicts that finite-size corrections are small; the result agrees within error bars with much larger

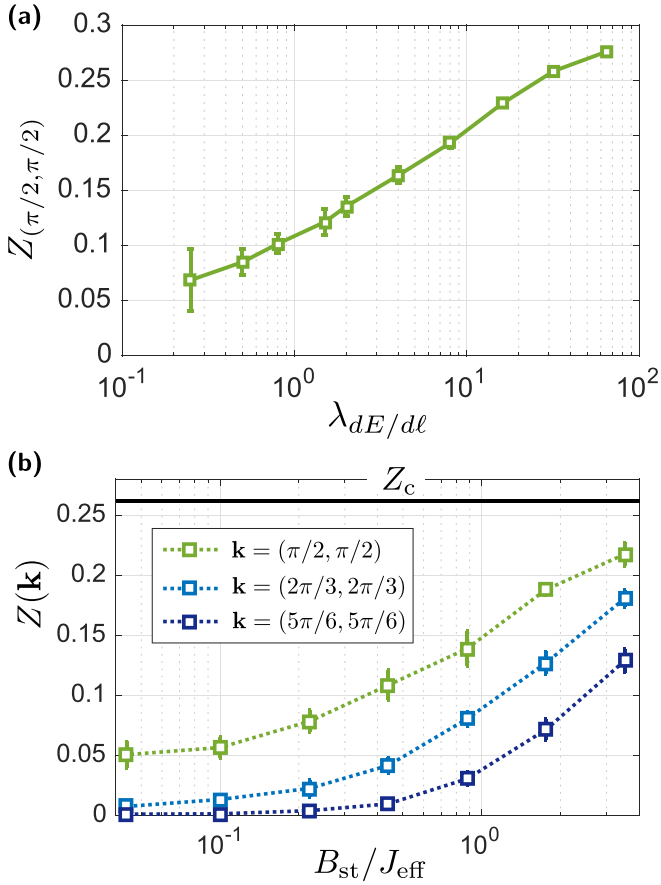

FIG. 17. Dependence of the quasiparticle weight on string tension and staggered magnetic field. (a) We calculate the quasiparticle residue $Z(\pi/2, \pi/2)$ from the trial wave function for different string length distributions. The latter are determined by the linear string tension $dE/d\ell = \lambda_{dE/d\ell} 2J(C_{\boldsymbol{e}_x+\boldsymbol{e}_y} - C_{\boldsymbol{e}_x})$ used in the FSA ansatz; large $\lambda_{dE/d\ell} \gg 1$ corresponds to short strings, and vice versa. We use parameters $B_{st}/J_{eff} = 0.44$ and $\Phi = 0.4\pi$ in a 12×12 system. For $t/J = 3$ the variational energy is minimized for $\lambda_{dE/d\ell}$ between 10^0 to 10^1 (see Ref. [35]). (b) The quasiparticle weight is calculated for different values of the staggered magnetic field B_{st}/J_{eff} in the trial wave function (12). For large staggered fields, the chargon, or string, contribution Z_c is approached. For weak staggered fields a strong momentum dependence is observed. We set $t = 3J$, $\Phi = 0.4\pi$, and worked in a 12×12 system.

12×12 and 20×20 systems. Since our DMRG and td-MPS studies are performed on multileg cylinders, we also considered an elongated 4×10 torus with our trial wave function. We find that this system also features no discernible finite-size corrections within the error bars. Taken together, these results suggest weak systematic effects of the elongated cylinder geometry for $t/J = 3$, while including sufficiently many lattice sites is important for obtaining a good approximation of the ideal 2D ground state. For larger values of $t/J > 3$, generally we expect finite-size effects to increase due to the growing string length.

We have also compared the ground-state quasiparticle weight Z obtained from DMRG for four- and six-leg cylinders (see Fig. 13). Going from $L_r = 4$ legs to $L_r = 6$ legs, we observe a slight reduction of the quasiparticle weight on the 1% level; see inset of Fig. 13 where the difference between the two cases is plotted for clarity (note the overall scale $\times 10^{-3}$). For the considered values of t/J, this observed finite-size effect is well below the finite-size variations found by exact diagonalization between systems with $N = 16$, 24, and 32 sites [26]. Moreover, in Fig. 3 we compare our DMRG results to quantum Monte Carlo simulations by Brunner *et al.* [28] for a 16×16 lattice and Mishchenko *et al.* [29] who considered 32×32 systems at a low inverse temperature of $\beta = 40/J$. The very good agreement of our DMRG results with the genuine 2D Monte Carlo data suggests that finite-size effects owing to the elongated cylinder geometry are weak for the considered values of t/J.

The third indicator we consider is the excitation gap to the first vibrational peak, plotted in Fig. 2. This is a useful quantity to consider since it goes beyond just the ground-state physics. For small J/t, we find very good agreement of our four-leg cylinder td-MPS results and 2D Monte Carlo predictions, within the typical peak widths indicated by error bars for the Monte Carlo calculations [29]. (Note that when $t \simeq J$ becomes comparable, it becomes increasingly more challenging within the given resolutions of DMRG and Monte Carlo methods to distinguish the vibrational from the ground-state peak in the spectrum. We believe this underlies the observed discrepancies for $t \simeq J$).

In summary, all finite-size scalings and benchmarks we can currently perform hint to small and controlled finite-size effects for the considered values of $t/J \leqslant 5$, caused by the elongated cylinder geometry we use in td-MPS and DMRG simulations. For larger values of t/J we observe that finite-size effects increase, as can be seen in the inset of Fig. 13. Such behavior is expected from the geometric string picture since the average string length and the extent of the magnetic polaron quickly increase with increasing t/J.

APPENDIX E: MEAN-FIELD APPROXIMATION AND SPINON STATISTICS

In this Appendix, we describe the phenomenology of the quasiparticle weight $Z_s(\boldsymbol{k})$ expected from two different mean-field descriptions. Only the fermionic theory is consistent with numerical results.

1. Fermionic spinons

In this approach, we assume that the constituting spinons $\hat{f}_{j,\sigma}$ introduced in Eq. (3) obey fermionic statistics. In our derivation of the mean-field expression $Z_s^{MF}(\boldsymbol{k})$ in Eq. (16) of the main text, we first assume that only $\Sigma = 0$ leads to a nonvanishing contribution:

$$\begin{aligned}
&\langle \Psi_{sc}(\boldsymbol{k}) | \hat{f}_{\boldsymbol{k},\sigma} \hat{\mathcal{P}}_{GW} \big| \Psi_{MF}^{SF+N} \big\rangle \\
&\approx \psi^*_{\Sigma=0} \sum_{j^s} \frac{u^{(j^s)}_{\boldsymbol{k},\sigma,-} e^{-i\boldsymbol{k}\cdot j^s}}{L/\sqrt{2}} \big\langle \Psi_{MF}^{SF+N} \big| \hat{f}^\dagger_{j^s,\sigma} \hat{\mathcal{P}}_{GW} \hat{f}_{\boldsymbol{k},\sigma} \hat{\mathcal{P}}_{GW} \big| \Psi_{MF}^{SF+N} \big\rangle \\
&= \psi^*_{\Sigma=0} \big\langle \Psi_{MF}^{SF+N} \big| \hat{f}^\dagger_{\boldsymbol{k},\sigma,-} \hat{\mathcal{P}}_{GW} \hat{f}_{\boldsymbol{k},\sigma} \hat{\mathcal{P}}_{GW} \big| \Psi_{MF}^{SF+N} \big\rangle . \qquad \text{(E1)}
\end{aligned}$$

In the second step, we used

$$\hat{f}^{\dagger}_{\boldsymbol{k},\sigma,\mu} = \sum_{j} \frac{e^{-i\boldsymbol{k}\cdot\boldsymbol{j}}}{L/\sqrt{2}}\, u^{(j)}_{\boldsymbol{k},\sigma,\mu}\, \hat{f}^{\dagger}_{\boldsymbol{j},\boldsymbol{\sigma}}. \tag{E2}$$

Next, we drop the Gutzwiller projectors and approximate

$$\begin{aligned}&\left\langle \Psi^{\mathrm{SF+N}}_{\mathrm{MF}} \middle| \hat{f}^{\dagger}_{\boldsymbol{k},\sigma,-} \hat{\mathcal{P}}_{\mathrm{GW}} \hat{f}_{\boldsymbol{k},\sigma} \hat{\mathcal{P}}_{\mathrm{GW}} \middle| \Psi^{\mathrm{SF+N}}_{\mathrm{MF}} \right\rangle \\ &\quad\approx \left\langle \Psi^{\mathrm{SF+N}}_{\mathrm{MF}} \middle| \hat{f}^{\dagger}_{\boldsymbol{k},\sigma,-} \hat{f}_{\boldsymbol{k},\sigma} \middle| \Psi^{\mathrm{SF+N}}_{\mathrm{MF}} \right\rangle,\end{aligned} \tag{E3}$$

which yields the mean-field result (16) in the main text. Note that $\hat{f}_{\boldsymbol{k}+\boldsymbol{K},\sigma,-} \equiv \hat{f}_{\boldsymbol{k},\sigma,-}$, where $\boldsymbol{K}$ is the reciprocal lattice vector, but $\hat{f}_{\boldsymbol{k}+\boldsymbol{K},\sigma} \neq \hat{f}_{\boldsymbol{k},\sigma}$.

We use the following identities:

$$\hat{f}^{\dagger}_{\boldsymbol{k},\sigma} = \lambda^{+}_{\boldsymbol{k}} \hat{f}^{\dagger}_{\boldsymbol{k},\sigma,+} + \lambda^{-}_{\boldsymbol{k}} \hat{f}^{\dagger}_{\boldsymbol{k},\sigma,-}, \tag{E4}$$

$$\hat{f}^{\dagger}_{\boldsymbol{k}+\boldsymbol{K},\sigma} = \lambda^{+}_{\boldsymbol{k}+\boldsymbol{K}} \hat{f}^{\dagger}_{\boldsymbol{k},\sigma,+} + \lambda^{-}_{\boldsymbol{k}+\boldsymbol{K}} \hat{f}^{\dagger}_{\boldsymbol{k},\sigma,-}, \tag{E5}$$

where $\boldsymbol{k} \in \mathrm{MBZ}$ and the factors $\lambda^{\pm}$ are given by

$$\lambda^{\mu}_{\boldsymbol{k}} = \frac{1}{\sqrt{2}} \left(u^{(A)}_{\boldsymbol{k},\sigma,\mu} + u^{(B)}_{\boldsymbol{k},\sigma,\mu} \right)^{*}, \tag{E7}$$

$$\lambda^{\mu}_{\boldsymbol{k}+\boldsymbol{K}} = \frac{1}{\sqrt{2}} \left(u^{(A)}_{\boldsymbol{k},\sigma,\mu} - u^{(B)}_{\boldsymbol{k},\sigma,\mu} \right)^{*}; \tag{E8}$$

A and B denote sites $\boldsymbol{j}$ from the A and B sublattice, respectively, and $\mu = \pm$ is the band index. This leads to the result in Eq. (17) in the main text.

2. Bosonic spinons

In this approach, we assume that the constituting spinons $\hat{f}_{j,\sigma}$ introduced in Eq. (3) obey bosonic statistics. To avoid confusion, we replace $\hat{f}_{j,\sigma}$ by Schwinger bosons $\hat{a}_{j,\sigma}$ in the following. First, we introduce the bosonic analog of the trial wave function (12) in the main text. We start from the usual Holstein-Primakoff expansion $\hat{S}^{z}_{j} = (-1)^{j}(1/2 - \hat{a}^{\dagger}_{j}\hat{a}_{j})$, where $(-1)^{j} = (-1)^{j_x + j_y}$. This corresponds to a mean-field expansion around the condensates $\hat{a}_{j_A,\uparrow}, \hat{a}_{j_B,\downarrow} \to \alpha_{j_A,\uparrow}, \alpha_{j_B,\downarrow} = 1$. Here, $\boldsymbol{j}_{A,B}$ denote lattice sites from the A and B sublattices, respectively, and $\alpha_{j,\sigma}$ denotes coherent state amplitudes. The operators $\hat{a}_{j_A} = \hat{a}_{j_A,\downarrow}$ and $\hat{a}_{j_B} = \hat{a}_{j_B,\uparrow}$ describe spin flips of the antiferromagnet, giving rise to collective spin-wave excitations which carry spin $S = 1$.

The fluctuations $\hat{b}_{j,\uparrow} = \hat{a}_{j_A,\uparrow}$ for $\boldsymbol{j} = \boldsymbol{j}_A \equiv \boldsymbol{j}_{\uparrow}$ and $\hat{b}_{j,\downarrow} = \hat{a}_{j_B,\downarrow}$ for $\boldsymbol{j} = \boldsymbol{j}_B \equiv \boldsymbol{j}_{\downarrow}$ around the condensate describe vacancies in the classical Néel state around which we expand in the Holstein-Primakoff approach. Hence, they correspond to spin-$\frac{1}{2}$ excitations, and we interpret them as bosonic spinons. This leads us to the following form of spinon-chargon trial states:

$$|\Psi_{\mathrm{sc}}(\boldsymbol{k})\rangle = \sum_{\boldsymbol{j}^{s}_{\sigma}} \frac{e^{i\boldsymbol{k}\cdot\boldsymbol{j}^{s}}}{L/\sqrt{2}} \sum_{\Sigma} \psi_{\Sigma}\, \hat{G}_{\Sigma}\, \hat{\mathcal{P}}_{\mathrm{GW}}\, \hat{b}_{j^{s},\sigma} \left| \Psi^{\mathrm{SB}}_{\mathrm{MF}} \right\rangle \tag{E9}$$

[cf. Eq. (12)]. Here, $\sum_{\boldsymbol{j}^{s}_{\sigma}}$ denotes a sum over all sites from sublattice A for $\sigma = \uparrow$ and B for $\sigma = \downarrow$. As in the fermionic case, it holds $|\Psi_{\mathrm{sc}}(\boldsymbol{k} + \boldsymbol{K})\rangle = |\Psi_{\mathrm{sc}}(\boldsymbol{k})\rangle$ up to an overall phase and for reciprocal lattice vectors $\boldsymbol{K}$. The bosonic mean-field description of the half-filled Heisenberg AFM is given by

$$\left| \Psi^{\mathrm{SB}}_{\mathrm{MF}} \right\rangle = \prod_{j} (|\alpha_{j_A,\uparrow} = 1\rangle |\alpha_{j_B,\downarrow} = 1\rangle) \otimes |\Psi_{\mathrm{fluc}}\rangle, \tag{E10}$$

where $\prod_{j}$ is a product over all unit cells $\boldsymbol{j}$, each consisting of a site $\boldsymbol{j}_A$ from the A and a site $\boldsymbol{j}_B$ from the B sublattice. $|\Psi_{\mathrm{fluc}}\rangle$ denotes the bosonic Gaussian state of fluctuations in the Hilbert space of $\hat{a}_{j_A,\downarrow}$ and $\hat{a}_{j_B,\uparrow}$ Schwinger bosons; $|\alpha_{j,\sigma}\rangle$ denotes a coherent state of Schwinger bosons with complex amplitude $\alpha_{j,\sigma}$.

In the calculation of the quasiparticle residue within the mean-field theory we assume, as in the fermionic case, that only the trivial string configuration $\Sigma = 0$ contributes. Dropping the Gutzwiller projection leads to the following bosonic mean-field expression:

$$Z^{\mathrm{MF,B}}(\boldsymbol{k}) = Z_{\mathrm{c}} \sum_{\sigma} \left| \left\langle \Psi^{\mathrm{SB}}_{\mathrm{MF}} \middle| \hat{a}^{\dagger}_{\boldsymbol{k},\eta_{\sigma},\sigma} \hat{a}_{\boldsymbol{k},\sigma} \middle| \Psi^{\mathrm{SB}}_{\mathrm{MF}} \right\rangle \right|^{2} \tag{E11}$$

[cf. Eq. (16)]. Here, we introduced

$$\hat{a}_{\boldsymbol{k},\mu,\sigma} = \frac{\sqrt{2}}{L} \sum_{\boldsymbol{j}_{\mu}} e^{i\boldsymbol{k}\cdot\boldsymbol{j}_{\mu}} \hat{a}_{\boldsymbol{j}_{\mu},\sigma}, \tag{E12}$$

for $\mu = A, B$ and defined

$$\eta_{\sigma} = \begin{cases} A, & \sigma = \uparrow \\ B, & \sigma = \downarrow \end{cases}. \tag{E13}$$

Hence, $\hat{a}^{\dagger}_{\boldsymbol{k},\eta_{\sigma},\sigma}$ only involves the spinon operators $\hat{b}_{j,\sigma}$ but not the spin-flip operators $\hat{a}_{j}$.

To calculate $Z^{\mathrm{MF,B}}(\boldsymbol{k})$ in Eq. (E11) we note that the Schwinger-boson mean-field state (E10) can be written

$$\left| \Psi^{\mathrm{SB}}_{\mathrm{MF}} \right\rangle = |\alpha_{\boldsymbol{k}=0,A,\uparrow}\rangle |\alpha_{\boldsymbol{k}=0,B,\downarrow}\rangle \otimes |\Psi_{\mathrm{fluc}}\rangle, \tag{E14}$$

with coherent amplitudes $\alpha_{\boldsymbol{k}=0,A,\uparrow} = \alpha_{\boldsymbol{k}=0,B,\downarrow} = L/\sqrt{2}$, i.e., the free spinons condense at $\boldsymbol{k} = 0$ in the mean-field theory. This condensate is the bosonic counterpart of the Fermi sea formed by constituting spinons in the fermionic mean-field theory.

The rest of the bosonic mean-field calculation is straightforward. Because $\hat{a}_{\boldsymbol{k},\mu,\sigma} = \hat{a}_{\boldsymbol{k}+\boldsymbol{K},\mu,\sigma}$ up to an overall phase for the reciprocal lattice vector $\boldsymbol{K} = (\pi, \pi)$, we find that

$$Z^{\mathrm{MF,B}}(\boldsymbol{k}) = Z_{\mathrm{c}} \frac{L^{2}}{2} (\delta(\boldsymbol{k}) + \delta(\boldsymbol{k} - \boldsymbol{K})). \tag{E15}$$

This directly leads to

$$Z^{\mathrm{MF,B}}_{\mathrm{s}}(\boldsymbol{k}) \propto (\delta(\boldsymbol{k}) + \delta(\boldsymbol{k} - \boldsymbol{\pi})), \quad \boldsymbol{\pi} = (\pi, \pi). \tag{E16}$$

Instead of the Fermi sea revealed in the fermionic mean-field theory, we expect two delta distributions at $\boldsymbol{k} = (0, 0)$ and $\boldsymbol{k} = (\pi, \pi)$. Beyond the mean-field ansatz, the Gutzwiller projection is expected to lead to substantial broadening of these delta-function peaks. While this may explain some of the numerical observations, it cannot explain the striking suppression of spectral weight around $\boldsymbol{k} = (\pi, \pi)$ observed numerically. While it is difficult to rule out bosonic descriptions of spinons completely, we conclude that strong interactions between the bosons would be required to explain the observed distribution of spectral weight across the Brillouin zone.

[1] A. Damascelli, Z. Hussain, and Z.-X. Shen, Angle-resolved photoemission studies of the cuprate superconductors, Rev. Mod. Phys. **75**, 473 (2003).

[2] J. M. Luttinger, An exactly soluble model of a many-fermion system, J. Math. Phys. **4**, 1154 (1963).

[3] E. H. Lieb and F. Y. Wu, Absence of Mott Transition in an Exact Solution of the Short-Range, One-Band Model in One Dimension, Phys. Rev. Lett. **20**, 1445 (1968).

[4] M. Ogata and H. Shiba, Bethe-ansatz wave function, momentum distribution, and spin correlation in the one-dimensional strongly correlated hubbard model, Phys. Rev. B **41**, 2326 (1990).

[5] K. J. von Szczepanski, P. Horsch, W. Stephan, and M. Ziegler, Single-particle excitations in a quantum antiferromagnet, Phys. Rev. B **41**, 2017 (1990).

[6] Z. Y. Weng, D. N. Sheng, and C. S. Ting, Spin-charge separation in the *t-J* model: Magnetic and transport anomalies, Phys. Rev. B **52**, 637 (1995).

[7] C. Kim, A. Y. Matsuura, Z.-X. Shen, N. Motoyama, H. Eisaki, S. Uchida, T. Tohyama, and S. Maekawa, Observation of Spin-Charge Separation in One-Dimensional $SrCuO_2$, Phys. Rev. Lett. **77**, 4054 (1996).

[8] C. Kim, Z.-X. Shen, N. Motoyama, H. Eisaki, S. Uchida, T. Tohyama, and S. Maekawa, Separation of spin and charge excitations in one-dimensional $SrCuO_2$, Phys. Rev. B **56**, 15589 (1997).

[9] R. N. Bannister and N. d'Ambrumenil, Spectral functions of half-filled one-dimensional hubbard rings with varying boundary conditions, Phys. Rev. B **61**, 4651 (2000).

[10] M. Sing, U. Schwingenschlögl, R. Claessen, P. Blaha, J. M. P. Carmelo, L. M. Martelo, P. D. Sacramento, M. Dressel, and C. S. Jacobsen, Electronic structure of the quasi-one-dimensional organic conductor TTF-TCNQ, Phys. Rev. B **68**, 125111 (2003).

[11] T. Giamarchi, *Quantum Physics in One Dimension* (Oxford University Press, Oxford, 2003).

[12] P. A. Lee, N. Nagaosa, and X.-G. Wen, Doping a mott insulator: Physics of high-temperature superconductivity, Rev. Mod. Phys. **78**, 17 (2006).

[13] B. O. Wells, Z. X. Shen, A. Matsuura, D. M. King, M. A. Kastner, M. Greven, and R. J. Birgeneau, *e* versus k Relations and Many Body Effects in the Model Insulating Copper Oxide $Sr_2CuO_2Cl_2$, Phys. Rev. Lett. **74**, 964 (1995).

[14] F. Ronning, K. M. Shen, N. P. Armitage, A. Damascelli, D. H. Lu, Z.-X. Shen, L. L. Miller, and C. Kim, Anomalous high-energy dispersion in angle-resolved photoemission spectra from the insulating cuprate $Ca_2CuO_2Cl_2$, Phys. Rev. B **71**, 094518 (2005).

[15] J. Graf, G.-H. Gweon, K. McElroy, S. Y. Zhou, C. Jozwiak, E. Rotenberg, A. Bill, T. Sasagawa, H. Eisaki, S. Uchida, H. Takagi, D.-H. Lee, and A. Lanzara, Universal High Energy Anomaly in the Angle-Resolved Photoemission Spectra of High Temperature Superconductors: Possible Evidence of Spinon and Holon Branches, Phys. Rev. Lett. **98**, 067004 (2007).

[16] S. Schmitt-Rink, C. M. Varma, and A. E. Ruckenstein, Spectral Function of Holes in a Quantum Antiferromagnet, Phys. Rev. Lett. **60**, 2793 (1988).

[17] C. L. Kane, P. A. Lee, and N. Read, Motion of a single hole in a quantum antiferromagnet, Phys. Rev. B **39**, 6880 (1989).

[18] S. Sachdev, Hole motion in a quantum néel state, Phys. Rev. B **39**, 12232 (1989).

[19] V. Elser, D. A. Huse, B. I. Shraiman, and E. D. Siggia, Ground state of a mobile vacancy in a quantum antiferromagnet: Small-cluster study, Phys. Rev. B **41**, 6715 (1990).

[20] E. Dagotto, R. Joynt, A. Moreo, S. Bacci, and E. Gagliano, Strongly correlated electronic systems with one hole: Dynamical properties, Phys. Rev. B **41**, 9049 (1990).

[21] G. Martinez and P. Horsch, Spin polarons in the *t-J* model, Phys. Rev. B **44**, 317 (1991).

[22] A. Auerbach and B. E. Larson, Small-Polaron Theory of Doped Antiferromagnets, Phys. Rev. Lett. **66**, 2262 (1991).

[23] Z. Liu and E. Manousakis, Dynamical properties of a hole in a heisenberg antiferromagnet, Phys. Rev. B **45**, 2425 (1992).

[24] M. Boninsegni and E. Manousakis, Green's-function monte carlo study of the *t-J* model, Phys. Rev. B **46**, 560 (1992).

[25] M. Boninsegni and E. Manousakis, Variational description of a quasihole excitation in a quantum antiferromagnet, Phys. Rev. B **45**, 4877 (1992).

[26] P. W. Leung and R. J. Gooding, Dynamical properties of the single-hole *t-J* model on a 32-site square lattice, Phys. Rev. B **52**, R15711 (1995).

[27] O. A. Starykh, O. F. de Alcantara Bonfim, and G. F. Reiter, Self-consistent born approximation for the hole motion in the three-band model: A comparison with photoemission experiments, Phys. Rev. B **52**, 12534 (1995).

[28] M. Brunner, F. F. Assaad, and A. Muramatsu, Single-hole dynamics in the $t-J$ model on a square lattice, Phys. Rev. B **62**, 15480 (2000).

[29] A. S. Mishchenko, N. V. Prokof'ev, and B. V. Svistunov, Single-hole spectral function and spin-charge separation in the $t-J$ model, Phys. Rev. B **64**, 033101 (2001).

[30] S. R. White and I. Affleck, Density matrix renormalization group analysis of the nagaoka polaron in the two-dimensional $t-J$ model, Phys. Rev. B **64**, 024411 (2001).

[31] G. Sangiovanni, A. Toschi, E. Koch, K. Held, M. Capone, C. Castellani, O. Gunnarsson, S.-K. Mo, J. W. Allen, H.-D. Kim, A. Sekiyama, A. Yamasaki, S. Suga, and P. Metcalf, Static versus dynamical mean-field theory of mott antiferromagnets, Phys. Rev. B **73**, 205121 (2006).

[32] E. Manousakis, String excitations of a hole in a quantum antiferromagnet and photoelectron spectroscopy, Phys. Rev. B **75**, 035106 (2007).

[33] F. Mezzacapo, Variational study of a mobile hole in a two-dimensional quantum antiferromagnet using entangled-plaquette states, Phys. Rev. B **83**, 115111 (2011).

[34] J. Koepsell, J. Vijayan, P. Sompet, F. Grusdt, T. A. Hilker, E. Demler, G. Salomon, I. Bloch, and C. Gross, Imaging magnetic polarons in the doped fermi-hubbard model, Nature (London) **572**, 358 (2019).

[35] F. Grusdt, A. Bohrdt, and E. Demler, Microscopic spinon-chargon theory of magnetic polarons in the t-j model, Phys. Rev. B **99**, 224422 (2019).

[36] T. Cuk, D. H. Lu, X. J. Zhou, Z.-X. Shen, T. P. Devereaux, and N. Nagaosa, A review of electron-phonon coupling seen in the high-tc superconductors by angle-resolved photoemission studies (arpes), Phys. Status Solidi B **242**, 11 (2005).

[37] S. Kar and E. Manousakis, Finite-temperature spectral function of a hole in a quantum antiferromagnet and the role of phonons, Phys. Rev. B **78**, 064508 (2008).

[38] P. A. Lee, From high temperature superconductivity to quantum spin liquid: Progress in strong correlation physics, Rep. Prog. Phys. **71**, 012501 (2008).

[39] K. M. Shen, F. Ronning, D. H. Lu, F. Baumberger, N. J. C. Ingle, W. S. Lee, W. Meevasana, Y. Kohsaka, M. Azuma, M. Takano, H. Takagi, and Z.-X. Shen, Nodal quasiparticles and antinodal charge ordering in $Ca_{2-x}Na_xCuO_2Cl_2$, Science **307**, 901 (2005).

[40] J. M. Luttinger, Fermi surface and some simple equilibrium properties of a system of interacting fermions, Phys. Rev. **119**, 1153 (1960).

[41] M. Oshikawa, Topological Approach to Luttinger's Theorem and the Fermi Surface of a Kondo Lattice, Phys. Rev. Lett. **84**, 3370 (2000).

[42] D. Chowdhury and S. Sachdev, The enigma of the pseudogap phase of the cuprate superconductors, *Quantum Criticality in Condensed Matter* (World Scientific, Singapore, 2015), pp. 1–43.

[43] S. Sachdev and D. Chowdhury, The novel metallic states of the cuprates: Topological fermi liquids and strange metals, Prog. Theor. Exp. Phys. **2016**, 12C102 (2016).

[44] T. K. Lee and S. Feng, Doping dependence of antiferromagnetism in La_2CuO_4: A numerical study based on a resonating-valence-bond state, Phys. Rev. B **38**, 11809 (1988).

[45] B. Dalla Piazza, M. Mourigal, N. B. Christensen, G. J. Nilsen, P. Tregenna-Piggott, T. G. Perring, M. Enderle, D. F. McMorrow, D. A. Ivanov, and H. M. Ronnow, Fractional excitations in the square-lattice quantum antiferromagnet, Nat. Phys. **11**, 62 (2015).

[46] A. Bohrdt, C. S. Chiu, G. Ji, M. Xu, D. Greif, M. Greiner, E. Demler, F. Grusdt, and M. Knap, Classifying snapshots of the doped hubbard model with machine learning, Nat. Phys. **15**, 921 (2019).

[47] C. S. Chiu, G. Ji, A. Bohrdt, M. Xu, M. Knap, E. Demler, F. Grusdt, M. Greiner, and D. Greif, String patterns in the doped hubbard model, Science **365**, 251 (2019).

[48] R. A. Hart, P. M. Duarte, T.-L. Yang, X. Liu, T. Paiva, E. Khatami, R. T. Scalettar, N. Trivedi, D. A. Huse, and R. G. Hulet, Observation of antiferromagnetic correlations in the hubbard model with ultracold atoms, Nature (London) **519**, 211 (2015).

[49] D. Greif, T. Uehlinger, G. Jotzu, L. Tarruell, and T. Esslinger, Short-range quantum magnetism of ultracold fermions in an optical lattice, Science **340**, 1307 (2013).

[50] L. W. Cheuk, M. A. Nichols, K. R. Lawrence, M. Okan, H. Zhang, E. Khatami, N. Trivedi, T. Paiva, M. Rigol, and M. W. Zwierlein, Observation of spatial charge and spin correlations in the 2d fermi-hubbard model, Science **353**, 1260 (2016).

[51] M. Boll, T. A. Hilker, G. Salomon, A. Omran, J. Nespolo, L. Pollet, I. Bloch, and C. Gross, Spin- and density-resolved microscopy of antiferromagnetic correlations in fermi-hubbard chains, Science **353**, 1257 (2016).

[52] A. Mazurenko, C. S. Chiu, G. Ji, M. F. Parsons, M. Kanasz-Nagy, R. Schmidt, F. Grusdt, E. Demler, D. Greif, and M. Greiner, A cold-atom fermi-hubbard antiferromagnet, Nature (London) **545**, 462 (2017).

[53] I. Affleck and B. I. Halperin, On a renormalization group approach to dimensional crossover, J. Phys. A: Math. Gen. **29**, 2627 (1996).

[54] F. Kagawa, K. Miyagawa, and K. Kanoda, Unconventional critical behavior in a quasi-two-dimensional organic conductor, Nature (London) **436**, 534 (2005).

[55] C. Kollath, M. Köhl, and T. Giamarchi, Scanning tunneling microscopy for ultracold atoms, Phys. Rev. A **76**, 063602 (2007).

[56] J. T. Stewart, J. P. Gaebler, and D. S. Jin, Using photoemission spectroscopy to probe a strongly interacting fermi gas, Nature (London) **454**, 744 (2008).

[57] D. Greif, L. Tarruell, T. Uehlinger, R. Jördens, and T. Esslinger, Probing Nearest-Neighbor Correlations of Ultracold Fermions in an Optical Lattice, Phys. Rev. Lett. **106**, 145302 (2011).

[58] P. Torma, Physics of ultracold fermi gases revealed by spectroscopies, Phys. Scr. **91**, 043006 (2016).

[59] A. Bohrdt, D. Greif, E. Demler, M. Knap, and F. Grusdt, Angle-resolved photoemission spectroscopy with quantum gas microscopes, Phys. Rev. B **97**, 125117 (2018).

[60] P. T. Brown, E. Guardado-Sanchez, B. M. Spar, E. W. Huang, T. P. Devereaux, and W. S. Bakr, Angle-resolved photoemission spectroscopy of a fermi-hubbard system, Nat. Phys. **16**, 26 (2020).

[61] M. P. Zaletel, R. S. K. Mong, C. Karrasch, J. E. Moore, and F. Pollmann, Time-evolving a matrix product state with long-ranged interactions, Phys. Rev. B **91**, 165112 (2015).

[62] S. Paeckel, T. Köhler, A. Swoboda, S. R. Manmana, U. Schollwöck, and C. Hubig, Time-evolution methods for matrix-product states, Ann. Phys. (NY) **411**, 167998 (2019).

[63] J. A. Kjäll, M. P. Zaletel, R. S. K. Mong, J. H. Bardarson, and F. Pollmann, Phase diagram of the anisotropic spin-2 XXZ model: Infinite-system density matrix renormalization group study, Phys. Rev. B **87**, 235106 (2013).

[64] M. Gohlke, R. Verresen, R. Moessner, and F. Pollmann, Dynamics of the Kitaev-Heisenberg Model, Phys. Rev. Lett. **119**, 157203 (2017).

[65] R. Verresen, F. Pollmann, and R. Moessner, Quantum dynamics of the square-lattice heisenberg model, Phys. Rev. B **98**, 155102 (2018).

[66] F. Grusdt, M. Kánasz-Nagy, A. Bohrdt, C. S. Chiu, G. Ji, M. Greiner, D. Greif, and E. Demler, Parton Theory of Magnetic Polarons: Mesonic Resonances and Signatures in Dynamics, Phys. Rev. X **8**, 011046 (2018).

[67] A. Auerbach, *Interacting Electrons and Quantum Magnetism* (Springer, Berlin, 1998).

[68] Y. Nagaoka, Ferromagnetism in a narrow, almost half-filled *s* band, Phys. Rev. **147**, 392 (1966).

[69] S. White, Density-matrix algorithms for quantum renormalization groups, Phys. Rev. B **48**, 10345 (1993).

[70] D. N. Sheng, Y. C. Chen, and Z. Y. Weng, Phase String Effect in a Doped Antiferromagnet, Phys. Rev. Lett. **77**, 5102 (1996).

[71] L. N. Bulaevskii, E. L. Nagaev, and D. I. Khomskii, A new type of auto-localized state of a conduction electron in an antiferromagnetic semiconductor, J. Exp. Theor. Phys. **27**, 836 (1968) [Zh. Eksp. Teor. Fiz. **54**, 1562 (1968)].

[72] W. F. Brinkman and T. M. Rice, Single-particle excitations in magnetic insulators, Phys. Rev. B **2**, 1324 (1970).

[73] S. A. Trugman, Interaction of holes in a hubbard antiferromagnet and high-temperature superconductivity, Phys. Rev. B **37**, 1597 (1988).

[74] B. I. Shraiman and E. D. Siggia, Two-Particle Excitations in Antiferromagnetic Insulators, Phys. Rev. Lett. **60**, 740 (1988).

[75] O. A. Starykh and G. F. Reiter, Hole motion in the ising antiferromagnet: An application of the recursion method, Phys. Rev. B **53**, 2517 (1996).

[76] D. Golez, J. Bonca, M. Mierzejewski, and L. Vidmar, Mechanism of ultrafast relaxation of a photo-carrier in antiferromagnetic spin background, Phys. Rev. B **89**, 165118 (2014).

[77] K. Bieniasz, P. Wrzosek, A. M. Oles, and K. Wohlfeld, From "weak" to "strong" hole confinement in a mott insulator, SciPost Phys. **7**, 066 (2019).

[78] P. Beran, D. Poilblanc, and R. B. Laughlin, Evidence for composite nature of quasiparticles in the 2d *t-J* model, Nucl. Phys. B **473**, 707 (1996).

[79] R. B. Laughlin, Evidence for Quasiparticle Decay in Photoemission from Underdoped Cuprates, Phys. Rev. Lett. **79**, 1726 (1997).

[80] T. Senthil, S. Sachdev, and M. Vojta, Fractionalized Fermi Liquids, Phys. Rev. Lett. **90**, 216403 (2003).

[81] M. Punk, A. Allais, and S. Sachdev, Quantum dimer model for the pseudogap metal, Proc. Natl. Acad. Sci. U. S. A. **112**, 9552 (2015).

[82] P. W. Anderson, The resonating valence bond state in La_2CuO_4 and superconductivity, Science **235**, 1196 (1987).

[83] F. Grusdt, Z. Zhu, T. Shi, and E. Demler, Meson formation in mixed-dimensional *t-J* models, SciPost Phys. **5**, 057 (2018).

[84] G. Baskaran, Z. Zou, and P. W. Anderson, The resonating valence bond state and high-tc superconductivity - A mean field theory, Solid State Commun. **63**, 973 (1987).

[85] X.-Y. Song, C. Wang, A. Vishwanath, and Y.-C. He, Unifying description of competing orders in two-dimensional quantum magnets, Nat. Commun. **10**, 4254 (2019).

[86] T. Giamarchi and C. Lhuillier, Dispersion relation of a single hole in the *t-J* model determined by a variational monte carlo method, Phys. Rev. B **47**, 2775 (1993).

[87] X.-G. Wen and P. A. Lee, Theory of Underdoped Cuprates, Phys. Rev. Lett. **76**, 503 (1996).

[88] N. Read and D. M. Newns, A new functional integral formalism for the degenerate anderson model, J. Phys. C: Solid State Phys. **16**, 1055 (1983).

[89] P. Coleman, New approach to the mixed-valence problem, Phys. Rev. B **29**, 3035 (1984).

[90] P. Coleman, Mixed valence as an almost broken symmetry, Phys. Rev. B **35**, 5072 (1987).

[91] G. Kotliar and J. Liu, Superexchange mechanism and *d*-wave superconductivity, Phys. Rev. B **38**, 5142 (1988).

[92] D. Yoshioka, Slave-fermion mean field theory of the hubbard model, J. Phys. Soc. Jpn. **58**, 1516 (1989).

[93] A. Bohrdt, F. Grusdt, and M. Knap, Dynamical formation of a magnetic polaron in a two-dimensional quantum antiferromagnet, arXiv:1907.08214.

[94] C. Hubig, A. Bohrdt, M. Knap, F. Grusdt, and J. Ignacio Cirac, Evaluation of time-dependent correlators after a local quench in ipeps: hole motion in the *t-J* model, SciPost Phys. **8**, 021 (2020).

[95] F. Ferrari and F. Becca, Spectral signatures of fractionalization in the frustrated heisenberg model on the square lattice, Phys. Rev. B **98**, 100405 (2018).

[96] Z. Y. Weng, D. N. Sheng, Y.-C. Chen, and C. S. Ting, Phase string effect in the *t-J* model: General theory, Phys. Rev. B **55**, 3894 (1997).

[97] H. V. Kruis, I. P. McCulloch, Z. Nussinov, and J. Zaanen, Geometry and the hidden order of luttinger liquids: The universality of squeezed space, Phys. Rev. B **70**, 075109 (2004).

[98] Y. Wang, K. Wohlfeld, B. Moritz, C. J. Jia, M. van Veenendaal, K. Wu, C.-C. Chen, and T. P. Devereaux, Origin of strong dispersion in hubbard insulators, Phys. Rev. B **92**, 075119 (2015).

[99] While the staggered magnetic field $B_{\rm st}$ improves the ground-state energy for the half-filled Heisenberg AFM, it has been shown in [45] to cause an unphysical gap in the dynamical spin structure factor at momentum (π, π). The dynamical spin structure factor is a response involving a pair of two constituting spinons, which requires the inclusion of their mutual interactions. In this work we consider the one-spinon sector, where spinon-spinon interactions play no role. In our case, the staggered field does not lead to inconsistencies.

[100] A. L. Chernyshev and P. W. Leung, Holes in the $t-J_z$ model: A diagrammatic study, Phys. Rev. B **60**, 1592 (1999).

[101] C. Gros, Physics of projected wave functions, Ann. Phys. (NY) **189**, 53 (1989).

[102] The chargon and spinon dispersions are only defined up to an overall gauge choice shifting their momenta in opposite directions.

[103] X.-G. Wen, *Quantum Field Theory of Many-body Systems* (Oxford University Press, Oxford, 2004).

[104] L. Savary and L. Balents, Quantum spin liquids: A review, Rep. Prog. Phys. **80**, 016502 (2017).

[105] J. Knolle and R. Moessner, A field guide to spin liquids, Annu. Rev. Condens. Matter Phys. **10**, 451 (2019).

[106] A. Läuchli, and D. Poilblanc, Spin-Charge Separation in Two-Dimensional Frustrated Quantum Magnets, Phys. Rev. Lett. **92**, 236404 (2004).

[107] C. Lavalle, M. Arikawa, S. Capponi, F. F. Assaad, and A. Muramatsu, Antiholons in One-Dimensional *t-J* Models, Phys. Rev. Lett. **90**, 216401 (2003).

[108] S. Depenbrock, I. P. McCulloch, and U. Schollwöck, Nature of the Spin-Liquid Ground State of the $s = 1/2$ Heisenberg Model on the Kagome Lattice, Phys. Rev. Lett. **109**, 067201 (2012).

[109] S. Hu, W. Zhu, S. Eggert, and Y.-C. He, Dirac Spin Liquid on the Spin-1/2 Triangular Heisenberg Antiferromagnet, Phys. Rev. Lett. **123**, 207203 (2019).

[110] A. V. Gorshkov, S. R. Manmana, G. Chen, J. Ye, E. Demler, M. D. Lukin, and A. M. Rey, Tunable Superfluidity and Quantum Magnetism with Ultracold Polar Molecules, Phys. Rev. Lett. **107**, 115301 (2011).

[111] Z. Zhu and Z.-Y. Weng, Quasiparticle collapsing in an anisotropic $t-J$ ladder, Phys. Rev. B **92**, 235156 (2015).

[112] Z. Zhu, D. N. Sheng, and Z.-Y. Weng, Intrinsic translational symmetry breaking in a doped mott insulator, Phys. Rev. B **98**, 035129 (2018).